Draft version January 21, 2025
Typeset using LaTeX **twocolumn** style in AASTeX631

Beyond MESA Defaults: The Impact of Structural Resolution Uncertainty in p-mode Asteroseismology

Yaguang Li (李亚光) [⋆1] and Meridith Joyce[⋆2,3,4]

[1] *Institute for Astronomy, University of Hawai'i, 2680 Woodlawn Drive, Honolulu, HI 96822, USA*
[2] *University of Wyoming, 1000 E University Ave, Laramie, WY USA*
[3] *Konkoly Observatory, HUN-REN CSFK, Konkoly-Thege Miklós út 15-17, H-1121, Budapest, Hungary*
[4] *CSFK, MTA Centre of Excellence, Konkoly-Thege Miklós út 15-17, H-1121, Budapest, Hungary*

ABSTRACT

Observations of pressure modes (p-modes) in stars have enabled profound insights into stellar properties, and theoretical stellar evolution and oscillation models are integral to these inferences. However, modeling uncertainties are often overlooked, even as they can rival or exceed observational uncertainties. In this study, we quantify, for the first time, the impact of structural resolution choices in 1D stellar evolution calculations on predicted p-mode frequencies across the HR diagram, using `MESA` and `GYRE`. We present measurements of resolution-based modeling uncertainty for a range of solar-like, upper main-sequence, and Mira oscillators and compare these directly to TESS observational uncertainties. We demonstrate that resolution-driven uncertainties can significantly influence theoretical predictions and in some cases overwhelm observational uncertainties by orders of magnitude: while solar-like oscillators typically have fractional, resolution-based uncertainties at or below 1% of the test frequency, fractional uncertainties in Miras were as large as 20%. We also find that the location and morphology of the RGB bump and red clump are impacted substantially by resolution uncertainty. Stellar ages are impacted at the 10% level for young main-sequence stars, and the model-based correction factor for the $\Delta\nu$–$\sqrt{\rho}$ scaling relation is impacted at the 2% level. Our results underscore the need to incorporate modeling uncertainties into asteroseismic analyses and provide a reference framework for observers evaluating the reliability of theoretical models.

1. INTRODUCTION

Pressure modes, or p-modes, have been observed in stars across a broad spectrum of masses, stellar types, and evolutionary phases. Such oscillations serve as a powerful tool for stellar characterization, enabling the inference of sub-surface structural information that can reveal the inner workings of stellar interiors (Aerts 2021) and more reliably constrain fundamental properties like mass and age (Chaplin & Miglio 2013; Silva Aguirre et al. 2015; Kurtz 2022). Theoretical calculations from stellar evolution and stellar oscillation codes constitute a critical component of the data-to-parameter pipeline. However, such modeling instruments are rarely used with the same standards of consideration afforded to observational instruments.

For some well-characterized stars (e.g. α Centauri A & B, 16 Cyg A & B; Kjeldsen et al. 2005; de Meulenaer et al. 2010; Metcalfe et al. 2012; Davies et al. 2015; Joyce & Chaboyer 2018b), the precision on observed frequencies quoted for individual p-modes exceeds the reliability of frequencies predicted by stellar models by several orders of magnitude (e.g. Murphy et al. 2021; Cunha et al. 2021). Despite the fact that modeling uncertainty overwhelmingly dominates the error budget in most cases concerning fits to individual p-modes, modeling uncertainties are rarely incorporated into asteroseismic results.

One reason modeling uncertainty considerations are commonly avoided is that the concept of "modeling uncertainty" encompasses at least three different issues:

1. predictions differ across codes;

yaguangl@hawaii.edu

mjoyce8@uwyo.edu

⋆ These authors contributed equally to this manuscript.

2. predictions differ when physical assumptions are varied within the same code; and
3. predictions differ when numerics, such as spatial resolution, temporal resolution, or solution tolerance, are changed within the same code.

Several authors have examined the first of these, both in the context of fits to individual objects (Huber et al. 2024) and to quantify variance across codes independent of any particular target (Christensen-Dalsgaard et al. 2020). Other studies have focused on the second issue, often using observationally well-characterized objects to underscore the importance of the intrinsic uncertainty in our modeling *choices* relative to observational precision (e.g. Joyce & Chaboyer 2018a,b; Tayar et al. 2022; Ying et al. 2023; Joyce et al. 2023; Cinquegrana et al. 2023; Li et al. 2024b; L. M. Morales, J. Tayar & Z. R. Clayton, in preparation). The third of these issues is addressed in the form of convergence studies, typically relegated to the appendices of our most robust modeling efforts. Resolution and convergence studies are not as common as they should be, but even when they are performed, the results are necessarily specific to the regime of the problem. While convergence tests may reinforce the reliability of results over a limited domain of interest, they do not tell us much about the overall reliability of software instruments.

A complete characterization of modeling uncertainty would thus involve rigorously quantifying differences between tools, differences between physical assumptions, and differences between numerical choices. This is understandably perceived to be beyond the scope of most analyses, especially in the case of point 1, given that many software tools are closed-source (see Tedersoo et al. 2021). However, the danger of neglecting modeling uncertainty in our asteroseismic analyses worsens as observational precision improves and as our data-driven inferences become more contrived and less transparent (e.g. using machine learning for bulk parameter estimation).

The Modules for Experiments in Stellar Astrophysics (`MESA`; Paxton et al. 2011, 2013, 2015, 2018, 2019; Jermyn et al. 2023) software suite is widely used in conjunction with the `GYRE` stellar oscillation program (Townsend & Teitler 2013) to compute asteroseismic properties for stellar models. Thanks to space-based photometric missions like WIRE (Hacking et al. 1997), MOST (Matthews et al. 2000), CoRoT (Auvergne et al. 2009), Kepler (Borucki et al. 2010), and TESS (Ricker et al. 2015), astronomers are obtaining increasingly high-precision measurements of individual p-mode pulsation frequencies for stars whose modes can be reliably identified. This data climate demands a more realistic understanding of the uncertainty in theoretical frequency predictions. We therefore focus in this paper on one of many under-explored contributions to theoretical error budgets: structural resolution in 1D stellar evolution and oscillation calculations.

In this study, we quantify the impact of varying `MESA`'s structural resolution control, `delta_mesh_coeff`, on theoretical p-mode frequencies across the HR diagram. We compare frequencies for solar-like oscillators (surface turbulence-driven), upper-main sequence pulsators (κ-mechanism-driven, including δ Scutis), and Miras (κ-mechanism-driven), covering evolutionary regimes from the main sequence to the asymptotic giant branch.

In Section 2, we discuss our model grid and physical assumptions, describe our method for comparing evolutionary tracks with different structural resolution, and introduce our method for measuring the discrepancies in frequency and period caused by resolution choices. In Section 3, we present our resolution uncertainty calculations across the HR diagram. In Section 4, we compare this source of modeling uncertainty directly to *TESS* observational uncertainties for stars of the appropriate type. **It is intended that this section serve as a quick-look reference for observers interested in a first-order estimate of the reliability of models in the regime of their data.** In Section 5, we discuss how our uncertainty considerations would impact modern asteroseismic techniques. We conclude by making recommendations for best practices in future asteroseismic p-mode analyses in Section 6.

2. METHODS

Our analysis requires two self-consistent grids of seismic stellar evolutionary tracks computed under two different structural resolution assumptions, a means of defining evolutionarily-equivalent points along each pair of tracks, and definitions for the discrepancies in key asteroseismic quantities: frequency and period. We discuss each below.

2.1. *Stellar models*

We use `MESA` version 24.03.1 and `GYRE` version 7.2 (in adiabatic mode) to compute evolutionary and asteroseismic models. We focus on a small number of models representative of the types of stars most commonly studied with p-mode and mixed-mode (p and g) observational asteroseismology. We include solar-mass models spanning four metallicities, $[\mathrm{Fe/H}] = \{-2.0, -1.0, 0.0, +0.5\}$, and three higher-mass models at solar composition, with masses of $1.4, 2.5$ and $5.0 M_\odot$. The upper main-sequence pulsators (including δ Scutis) are represented by main-sequence models with $T_{\rm eff}$ greater than 6800 K. The Miras are represented by models with $\log L$ greater than

Physics Component	Description	Reference
Abundances	GS98	Grevesse & Sauval (1998)
Nuclear reaction network	`'pp_and_cno_extras_o18_ne22.net'` includes all isotopes necessary for hydrogen-burning chains	
Equation of State	`Skye` EOS, `Free` EOS	Jermyn et al. (2023)
Opacities	GS98 for default with GS98 compatible Low-T, and CO opacities	
Mixing Length Theory $\alpha_{\rm MLT}$	`'Henyey'`; appropriate for low optical depth fixed to 2.1	Henyey et al. (1965)
Atmospheric boundary conditions	Eddington $T-\tau$ `atm_T_tau_opacity`='varying'	Eddington (1926)
Heavy element diffusion	None	
Treatment of convective boundaries	predictive mixing algorithm	Paxton et al. (2018)
Convective overshoot	'step' for all regions $f = 0.02$ H_P $f_0 = 0.002$ H_P	
`MESA` numerical parameters	`varcontrol_target = 1e-4` `time_delta_coeff = 1.0` `use_gold_tolerances = .true.` `use_gold2_tolerances = .true.`	Jermyn et al. (2023)
`GYRE` parameters	`diff_scheme = 'MAGNUS_GL6'` `n_iter_max = 50` `inner_bound = 'REGULAR'` `outer_bound = 'JCD'`	Townsend & Teitler (2013)

Table 1. Summary of physical assumptions used in `MESA` and `GYRE` models.

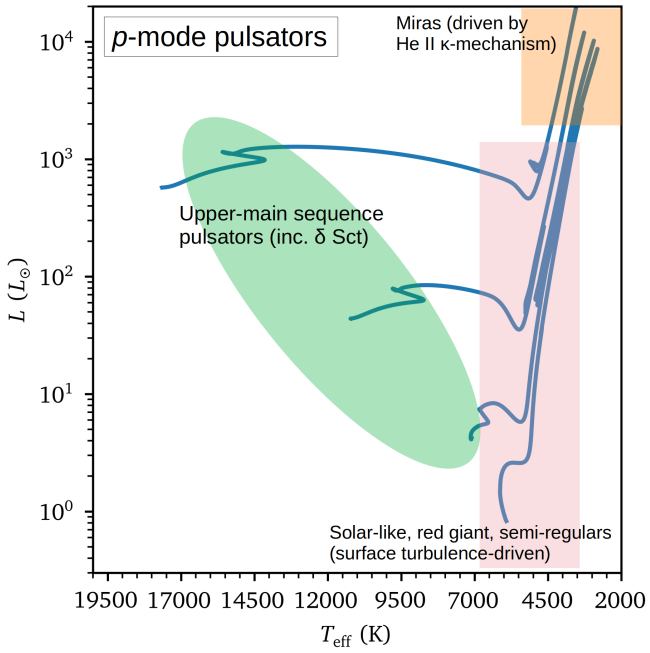

Figure 1. H–R diagram showing the three types of p-mode pulsators investigated in this study. Tracks shown have solar metallicity and masses of 1.0, 1.4, 2.0, and 5.0$M_\odot$, from lower right to upper left.

3.15. Solar-like oscillators are represented by cool main-sequence models and low-luminosity red giants. Figure 1 shows the p-mode variability regimes covered by our grid.

For all evolutionary calculations, we uniformly adopt a standard set of input physics, summarized in Table 1.[1] The structural resolution in `MESA` refers to the number of radial (Eulerian) or mass (Lagrangian) coordinates, or grid points, used in the calculation of stellar profiles. This is also called the `mesh` resolution. By default, `MESA` uses adaptive mesh refinement (AMR), meaning the model is "remeshed," or adjusted adaptively, from time step to time step (Paxton et al. 2011, Section 6). While a user may require that a particular, fixed number of grid points is preserved throughout the evolution of the model, this is not the optimal technique for dealing with models that can change significantly in complexity during their evolution, or which require non-uniform sampling of the stellar interior.

[1] The complete inlists will be made publicly available at time of acceptance at [url TBD]

Although the structural resolution can be controlled in this and a number of other ways, it is most commonly adjusted using the the `MESA` control `delta_mesh_coeff`. This control does not itself dictate the mesh resolution; rather, it is a *multiplier* on the default mesh resolution. By setting this control, the user specifies how much *more* (or less) resolved they would like the model to be beyond the default resolution determined by `MESA`'s AMR routine. A value of `delta_mesh_coeff` = 1.0 corresponds to `MESA`'s default structural resolution, and a value of `delta_mesh_coeff` = 0.1 corresponds to 10× the default structural resolution. As we will see, our results sharply demonstrate the inadequacy of using `MESA`'s default mesh resolution for most asteroseismic applications.

2.2. *Equivalent evolutionary points*

To study the impact of structural resolution on frequency (period) predictions as a function of evolutionary phase requires defining a metric of evolutionary equivalence that can be maintained across tracks with different properties. We begin with the Equivalent Evolutionary Phase, or EEP, method outlined in Dotter (2016), which ensures consistent definitions of evolutionary phase across models with different physical or numerical properties.

A set of "primary EEPs" comprises the following critical points in stellar evolution, defined by an index p and constructed such that the distance between two consecutive primary EEPs is 100:

EEP $p = 0$, Protostar: the initial point on the evolutionary track;

EEP $p = 100$, Zero-age main sequence: the point at which the central hydrogen mass fraction, `center_h1`, decreases by 0.0015 relative to its maximum value;

EEP $p = 200$, Intermediate-age main sequence: the point at which `center_h1` decreases to less than 0.3;

EEP $p = 300$, Terminal-age main sequence: the point at which `center_h1` decreases to less than 10^{-8};

EEP $p = 400$, Bottom of red-giant branch (RGB): the point at which the mass coordinate at the base of the surface convection zone penetrates to within 75% of the total stellar mass, or 0.25 $m/M_\odot$;

EEP $p = 500$, Onset of the RGB bump (if present): the point at which the effective temperature ($T_{\rm eff}$) begins to decrease along the RGB;

EEP $p = 600$, End of the RGB bump (if present): the point at which $T_{\rm eff}$ begins to increase again along the RGB, reversing direction after its descent;

EEP $p = 700$, Onset of helium flash: the point at which the helium-burning luminosity $L_{\rm He}$ exceeds 10^{-4} of the total nuclear-burning luminosity;

EEP $p = 800$, Zero-age core-helium burning phase: the point at which the central helium mass fraction `center_he4` decreases by 0.0015 from its maximum value;

EEP $p = 900$, Terminal-age core-helium burning phase: the point at which `center_he4` decreases to less than 0.05

EEP $p = 1000$, Onset of the AGB bump (if present): the point at which $T_{\rm eff}$ decreases for the first time along the asymptotic-giant branch (AGB);

EEP $p = 1100$, End of the AGB bump (if present): the point at which $T_{\rm eff}$ begins to increase along the AGB after its first descent;

EEP $p = 1200$, Onset of the first thermal pulse on the AGB: the point at which `center_he4` falls below 10^{-20}, and the hydrogen-to-helium burning luminosity ratio, $L_{\rm H}/L_{\rm He}$, exceeds 10;

EEP $p = 1200 + (n-1) \times 100$: Onset of the n-th AGB thermal pulse: subsequent episodes where $L_{\rm H}/L_{\rm He}$ temporarily drops below 10 and then rises above this threshold again.

This set of definitions differs somewhat from that presented in Dotter (2016), particularly in its denser coverage of the RGB and AGB phases. We do not consider the post-AGB or white dwarf cooling sequence here.

To enable the comparison of physical quantities at more precise locations, we next define sets of secondary EEPs between each pair of adjacent primary EEPs. We introduce an evolutionary distance metric, D, given by

$$D_{i+1} = D_i + \sqrt{\sum_{j=1}^{N_j} w_j (x_{j,i+1} - x_{j,i})^2}, \qquad (1)$$

where D_i is the cumulative distance at the i-th point on the evolutionary track, $x_{j,i}$ is the j-th physical quantity at the i-th point, and w_j are weighting factors applied to each physical quantity x_j, ensuring they are scaled appropriately for comparison. We adopt $w =$

$\{2.5, 9.0\}$ with $x = \{\texttt{log\_center\_T}, \texttt{log\_center\_Rho}\}$ as default. The weightings come from forcing $\log \rho_{\rm center}$ and $\log T_{\rm center}$ to a normalized scale, where $\log \rho_{\rm center}$ ranges from -3 to 6 across our models and $\log T_{\rm center}$ ranges from 6.0 to 8.5. To ensure that our results are not sensitive to the choice of metric, we tested an alternative definition of D, adopting $w = \{0.9, 4.6\}$ with $x = \{\texttt{log\_Teff}, \texttt{log\_L}\}$. This yields no significant differences in our results.

We compute D_i for every model (time step). The secondary EEPs $\{s_0 ... s_{100}\}$ are placed by min-max scaling D from 0 to 100 across each region demarcated by two adjacent primary EEPs:

$$s = [D - \min(D)/(\max(D) - \min(D))] \times 100. \quad (2)$$

The final EEPs we use as reference points for comparison between tracks with different resolutions are the result of adding the primary EEP p to the secondary EEP s. For example, if we are inspecting frequencies at secondary EEP $s = 53$ between the terminal-age main sequence ($p = 300$) and the bottom of the red giant branch ($p = 400$), the reference EEP is $p + s = 353$.

In subsequent analysis, we measure the frequency discrepancy at six representative evolutionary points on each track: the main sequence (MS) at EEP 187, the subgiant branch at EEP 303, the early red giant branch (RGB) at EEP 410, the late RGB at either EEP 665 (if the RGB bump is present) or 495 (if the RGB bump is not present), the core helium-burning phase (CHeB) at EEP 850, and the asymptotic giant branch (AGB) at EEP 1198. These henceforth serve as reference points for detailed examination of the models.

We define seven classes of models, each corresponding to a particular physical configuration adopted in the evolutionary track. Model Class 1 contains a main sequence, subgiant, early RGB, late RGB, core helium-burning, and AGB model with solar mass and solar metallicity. Model Class 2 assumes solar mass and a metal-enriched composition of [Fe/H] $= +0.5$ dex, representing the approximate upper limit on metal-enrichment in the Milky Way. Model Classes 3 and 4 use solar mass and metallicities of [Fe/H] $= -1.0$, and [Fe/H] $= -2.0$, respectively. Model Classes 5, 6, and 7 adopt solar composition and masses of 1.4, 2.5, and $5.0 M_\odot$, respectively. Table 2 provides a summary of critical stellar parameters—age, $T_{\rm eff}$, $\log L$, and $\log g$—at each reference EEP and corresponding evolutionary phase within each model class. Figure 2 shows the reference EEPs for each model class on the H–R diagram.

2.3. *Differences in Frequency and Period*

To describe the *absolute frequency discrepancy* between two points on models computed with identical input physics but different structural resolutions, we introduce the quantity $\varepsilon_{\texttt{dmesh}}$:

$$\varepsilon_{\texttt{dmesh}}(\text{EEP}) = |\nu_{\texttt{[dmesh=1.0]}}(\text{EEP}) - \nu_{\texttt{[dmesh=0.1]}}(\text{EEP})|, \quad (3)$$

where $\nu_{\texttt{[dmesh=1.0]}}(\text{EEP})$ refers to the test frequency ν measured at EEP on a track adopting the default (low) mesh resolution, $\texttt{delta\_mesh\_coeff} = 1.0$, and $\nu_{\texttt{[dmesh=0.1]}}(\text{EEP})$ refers to the frequency measured at EEP on the otherwise physically identical evolutionary track adopting $10\times$ the default structural resolution, $\texttt{delta\_mesh\_coeff} = 0.1$.

To determine which test frequency (mode) should be used to calculate $\varepsilon_{\texttt{dmesh}}$, we select frequencies in each domain representative of the modes most likely to be observed in stars of that type. We use p-mode frequencies for modes adjacent to $\nu_{\rm max}$ for solar-like oscillators, the $n = 5$ mode for upper main-sequence pulsators, and the fundamental ($n = 1$) mode for Miras. For all mode choices, spherical degree and azimuthal order are $l = 0$ and $m = 0$, respectively. The values of $\nu_{\rm max}$ are calculated as (Brown et al. 1991; Kjeldsen & Bedding 1995)

$$\nu_{\rm max} = \left(\frac{M}{M_\odot}\right)\left(\frac{R}{R_\odot}\right)^{-2}\left(\frac{T_{\rm eff}}{5777\,\text{K}}\right)^{-0.5} \times 3090\,\mu\text{Hz}. \quad (4)$$

The $\varepsilon_{\texttt{dmesh}}$ quantity is calculated at the preferred EEPs summarized in Table 2. For upper main-sequence and Mira oscillators, we use cubic interpolation to estimate the mode frequency for $n = 3$ or $n = 1$ as a function of EEP. For solar-like oscillators, the process involves three steps. First, cubic interpolation is used to estimate the mode frequencies of four radial (n) orders that bracket $\nu_{\rm max}$, as a function of EEP. Second, $\varepsilon_{\texttt{dmesh}}$ is evaluated for each of these orders at the desired EEPs (187, 303, 410, etc). Finally, cubic interpolation is performed again on $\varepsilon_{\texttt{dmesh}}$ as a function of mode frequency ν, and the final reported $\varepsilon_{\texttt{dmesh}}$ is evaluated at $\nu_{\rm max}$.

For longer-period variables, such as more massive red giants and AGB stars, it is more useful to express the discrepancy in terms of period rather than frequency. We thus introduce an analogous quantity representing the *absolute period discrepancy*, $\zeta_{\texttt{dmesh}}$, defined as

$$\zeta_{\texttt{dmesh}}(\text{EEP}) = |P_{\texttt{[dmesh=1.0]}}(\text{EEP}) - P_{\texttt{[dmesh=0.1]}}(\text{EEP})|. \quad (5)$$

The computation procedure is analogous to that of $\varepsilon_{\texttt{dmesh}}$, except periods are used in the interpolations instead of frequencies.

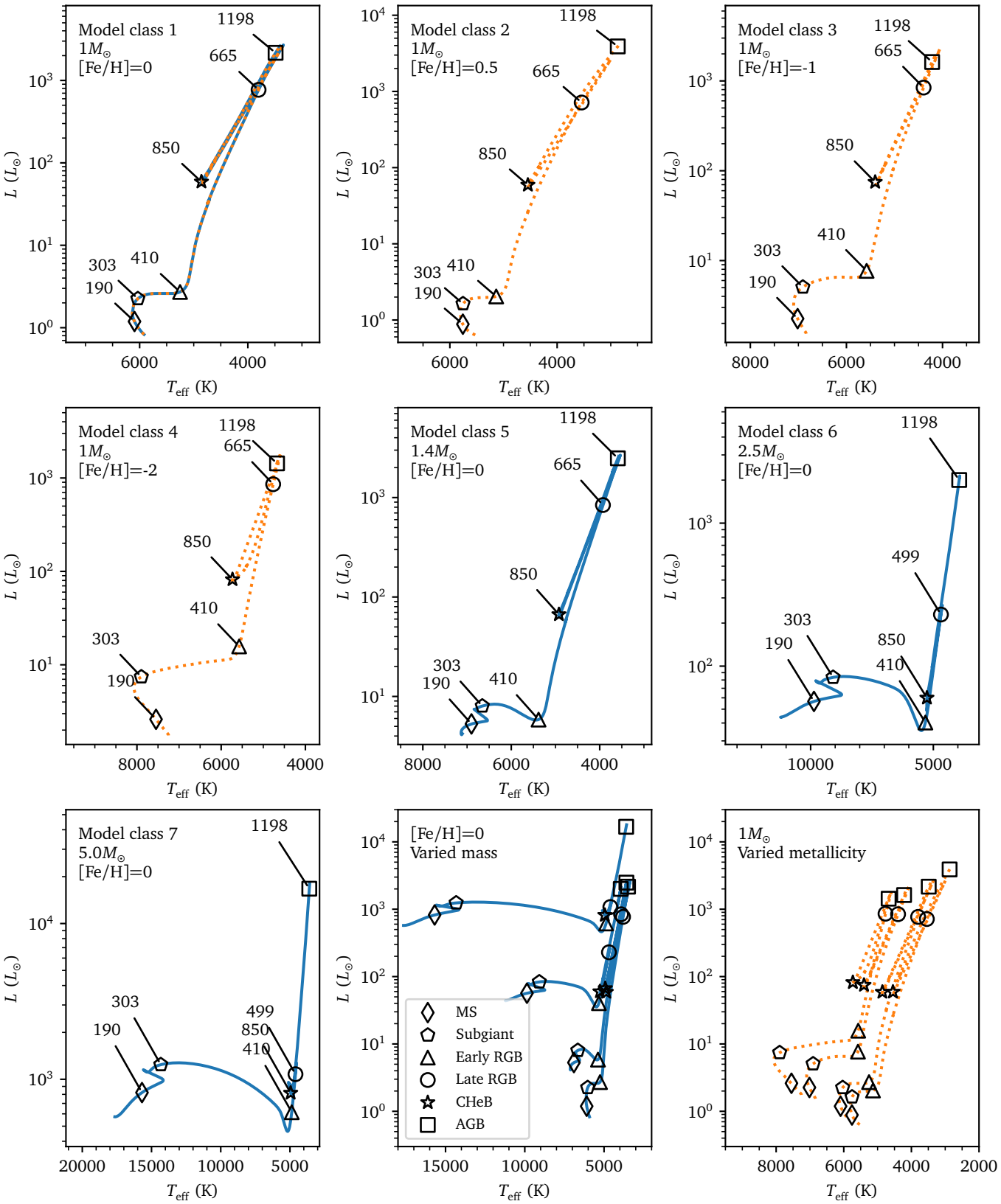

Figure 2. Panels 1 through 7 show the locations and indices of Equal Evolutionary Points (EEPs) for each model class, with the class indicated in the upper left. The ages and other fundamental parameters measured at these EEPs are summarized in Table 2.

Mass	**Z**	**[Fe/H]**	**Ev Phase**	**EEP**	**Age**	**Teff**	log**L**	log**g**	**see table...**
$M_\odot$		dex			Gyr	K	$L_\odot$	dex; cm/s^2	
Model Class 1: Solar-like									
1.0	0.0162	0.0	MS	187	3.934	6093	0.073	4.459	solar-like; Table 3
1.0	0.0162	0.0	subgiant	303	8.776	6036	0.350	4.165	solar-like; Table 3
1.0	0.0162	0.0	early RGB	410	9.794	5252	0.434	3.840	solar-like; Table 3
1.0	0.0162	0.0	late RGB	665	10.404	3802	2.886	0.826	solar-like; Table 3
1.0	0.0162	0.0	CHeB	850	10.452	4858	1.770	2.368	solar-like; Table 3
1.0	0.0162	0.0	AGB	1198	10.503	3487	3.335	0.228	Mira variables; Table 5
Model Class 2: metal-rich, solar mass									
1.0	0.0447	+0.5	MS	187	3.429	5755	-0.058	4.491	solar-like; Table 3
1.0	0.0447	+0.5	subgiant	303	9.451	5754	0.215	4.218	solar-like; Table 3
1.0	0.0447	+0.5	early RGB	410	10.681	5134	0.310	3.925	solar-like; Table 3
1.0	0.0447	+0.5	late RGB	665	11.330	3543	2.854	0.736	solar-like; Table 3
1.0	0.0447	+0.5	CHeB	850	11.378	4545	1.772	2.251	solar-like; Table 3
1.0	0.0447	+0.5	AGB	1198	11.438	2870	3.591	-0.367	Mira variables; Table 5
Model Class 3: metal-poor, solar mass									
1.0	0.0017	-1.0	MS	187	2.571	7010	0.347	4.428	Upper main sequence; Table 4
1.0	0.0017	-1.0	subgiant	303	5.508	6911	0.703	4.047	Upper main sequence; Table 4
1.0	0.0017	-1.0	early RGB	410	6.019	5580	0.886	3.494	solar-like; Table 3
1.0	0.0017	-1.0	late RGB	665	6.289	4394	2.926	1.038	solar-like; Table 3
1.0	0.0017	-1.0	CHeB	850	6.331	5403	1.873	2.450	solar-like; Table 3
1.0	0.0017	-1.0	AGB	1198	6.375	4217	3.210	0.682	Mira variables; Table 5
Model Class 4: very metal-poor, solar mass									
1.0	0.0002	-2.0	MS	187	2.372	7541	0.413	4.489	Upper main sequence; Table 4
1.0	0.0002	-2.0	subgiant	303	5.166	7891	0.872	4.109	Upper main sequence; Table 4
1.0	0.0002	-2.0	early RGB	410	5.497	5573	1.196	3.181	solar-like; Table 3
1.0	0.0002	-2.0	late RGB	665	5.650	4765	2.933	1.172	solar-like; Table 3
1.0	0.0002	-2.0	CHeB	850	5.688	5732	1.913	2.513	solar-like; Table 3
1.0	0.0002	-2.0	AGB	1198	5.729	4673	3.156	0.915	Mira variables; Table 5
Model Class 5: solar metallicity, $1.4M_\odot$									
1.4	0.0162	0.0	MS	187	1.462	6924	0.721	4.180	Upper main sequence; Table 4
1.4	0.0162	0.0	subgiant	303	2.461	6657	0.904	3.928	solar-like; Table 3
1.4	0.0162	0.0	early RGB	410	2.788	5381	0.768	3.695	solar-like; Table 3
1.4	0.0162	0.0	late RGB	665	3.125	3927	2.925	0.990	solar-like; Table 3
1.4	0.0162	0.0	CHeB	850	3.172	4923	1.823	2.484	solar-like; Table 3
1.4	0.0162	0.0	AGB	1198	3.222	3590	3.395	0.364	Mira variables; Table 5
Model Class 6: solar metallicity, $2.5M_\odot$									
2.5	0.0162	0.0	MS	187	0.321	9886	1.752	4.019	Upper main sequence; Table 4
2.5	0.0162	0.0	subgiant	303	0.470	9086	1.921	3.703	Upper main sequence; Table 4
2.5	0.0162	0.0	early RGB	410	0.484	5323	1.607	3.089	solar-like; Table 3
2.5	0.0162	0.0	late RGB	495	0.491	4722	2.322	2.165	solar-like; Table 3
2.5	0.0162	0.0	CHeB	850	0.593	5262	1.778	2.897	solar-like; Table 3
2.5	0.0162	0.0	AGB	1198	0.684	3947	3.301	0.875	Mira variables; Table 5
Model Class 7: solar metallicity, $5.0M_\odot$									
5.0	0.0162	0.0	MS	187	0.057	15752	2.911	3.970	Upper main sequence; Table 4
5.0	0.0162	0.0	subgiant	303	0.081	14326	3.094	3.622	Upper main sequence; Table 4
5.0	0.0162	0.0	early RGB	410	0.082	4871	2.789	2.053	solar-like; Table 3
5.0	0.0162	0.0	late RGB	495	0.082	4607	3.028	1.718	solar-like; Table 3
5.0	0.0162	0.0	CHeB	850	0.092	4952	2.912	1.958	solar-like; Table 3
5.0	0.0162	0.0	AGB	1198	0.100	3604	4.224	0.095	Mira variables; Table 5

Table 2. Overview of model classes and summary of fundamental parameters.

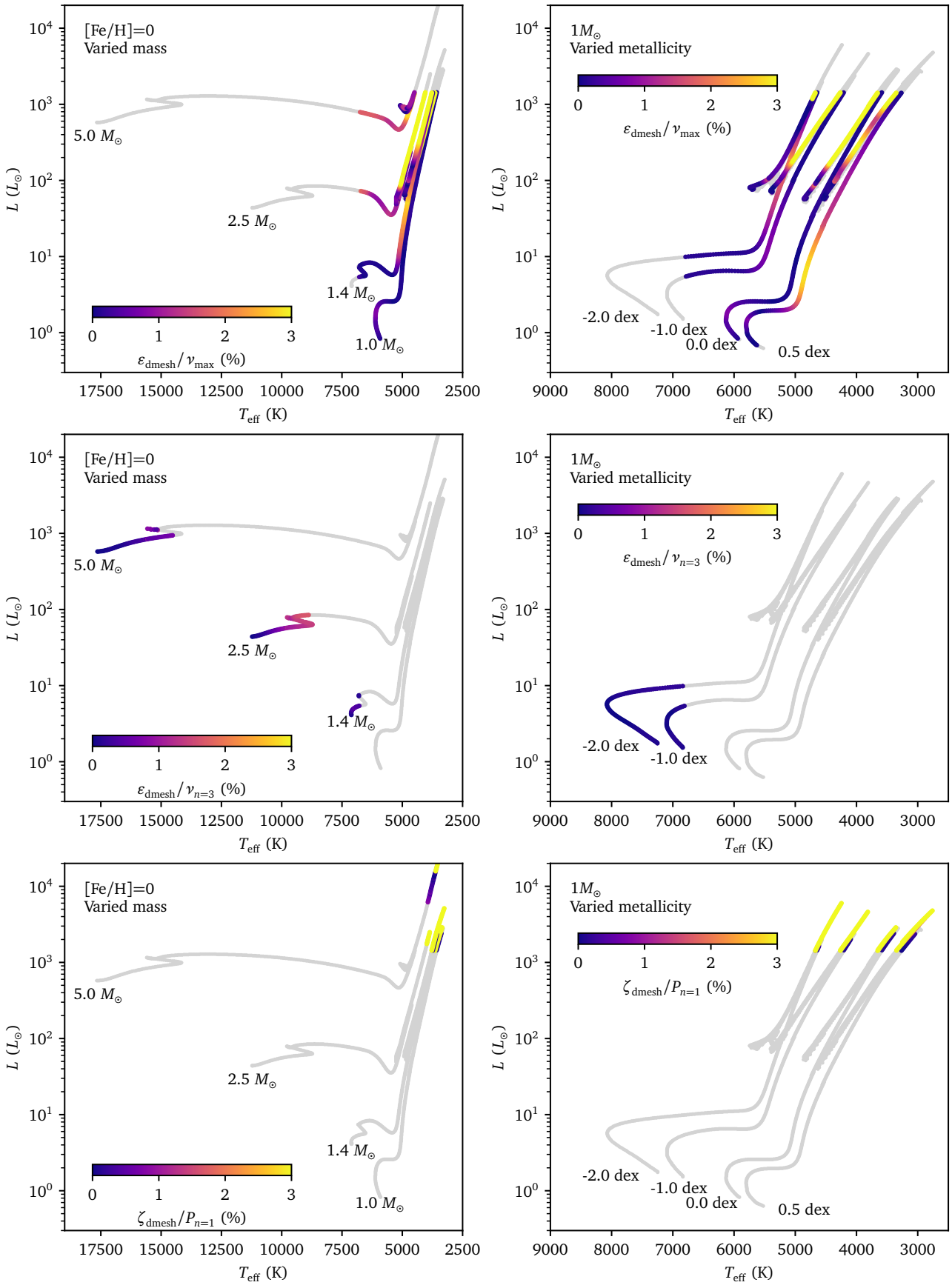

Figure 3. HR diagram color-coded by $\varepsilon_{\texttt{dmesh}}$ ($\zeta_{\texttt{dmesh}}$), the degree of discrepancy in representative test frequency $\nu_{\rm test}$ ($P_{\rm test}$). The left panel shows all models with solar metallicity but different masses, and the right panel with solar mass but different metallicites.

Mass	**Z**	**[Fe/H]**	**Ev Phase**	**EEP**	**Age**	n	$\nu_{\mathbf{max}}$	$\varepsilon_{\texttt{dmesh}}$	$\%\varepsilon_{\texttt{dmesh}}$
$M_\odot$		dex			Gyr	$\ell, m = 0$	μHz	μHz	$\varepsilon_{\texttt{dmesh}}/\nu_{\max}$
Model Class 1: Solar-like									
1.0	0.0162	0.0	MS	187	3.934	21,22	3158.2	11.9503	0.3784
1.0	0.0162	0.0	subgiant	303	8.776	17,18	1612.6	11.3307	0.7024
1.0	0.0162	0.0	early RGB	410	9.794	15,16	817.3	0.3393	0.0415
1.0	0.0162	0.0	late RGB	665	10.404	3,4	0.9	0.0005	0.0567
1.0	0.0162	0.0	CHeB	850	10.452	6,7	28.7	0.0606	0.2112
Model Class 2: metal-rich, solar mass									
1.0	0.0447	+0.5	MS	187	3.429	22,23	3491.8	2.8427	0.0814
1.0	0.0447	+0.5	subgiant	303	9.451	18,19	1863.8	12.9395	0.6937
1.0	0.0447	+0.5	early RGB	410	10.681	16,17	1005.1	9.2284	0.9183
1.0	0.0447	+0.5	late RGB	665	11.330	3,4	0.8	0.0028	0.3597
1.0	0.0447	+0.5	CHeB	850	11.378	6,7	22.6	0.0086	0.0381
Model Class 3: metal-poor, solar mass									
1.0	0.0017	-1.0	early RGB	410	6.019	12,13	357.3	2.0400	0.5711
1.0	0.0017	-1.0	late RGB	665	6.289	3,4	1.4	0.0011	0.0779
1.0	0.0017	-1.0	CHeB	850	6.331	6,7	32.8	0.0075	0.0230
Model Class 4: very metal-poor, solar mass									
1.0	0.0002	-2.0	early RGB	410	5.497	10,11	174.0	0.7560	0.4346
1.0	0.0002	-2.0	late RGB	665	5.650	3,4	1.8	0.0081	0.4400
1.0	0.0002	-2.0	CHeB	850	5.688	6,7	36.8	0.0484	0.1314
Model Class 5: solar metallicity, $1.4M_\odot$									
1.4	0.0162	0.0	subgiant	303	2.461	16,17	890.0	0.4952	0.0556
1.4	0.0162	0.0	early RGB	410	2.788	15,16	577.7	0.0585	0.0102
1.4	0.0162	0.0	late RGB	665	3.125	3,4	1.3	0.0072	0.5408
1.4	0.0162	0.0	CHeB	850	3.172	7,8	37.2	0.0313	0.0841
Model Class 6: solar metallicity, $2.5M_\odot$									
2.5	0.0162	0.0	early RGB	410	0.484	12,13	143.9	1.6080	1.1172
2.5	0.0162	0.0	late RGB	495	0.491	7,8	18.2	0.1367	0.7501
2.5	0.0162	0.0	CHeB	850	0.593	11,12	93.2	1.0864	1.1657
Model Class 7: solar metallicity, $5.0M_\odot$									
5.0	0.0162	0.0	early RGB	410	0.082	8,9	13.9	0.2760	1.9921
5.0	0.0162	0.0	late RGB	495	0.082	7,8	6.6	0.1851	2.8116
5.0	0.0162	0.0	CHeB	850	0.092	7,8	11.1	0.0072	0.0652

Table 3. Frequency discrepancies due to structural resolution, $\varepsilon_{\texttt{dmesh}}$, calculated for solar-like oscillators. $\varepsilon_{\texttt{dmesh}}$ is evaluated at $\nu_{\max}$. The mode with radial order n and spherical degree and azimuthal orders $\ell, m = 0$ nearest to $\nu_{\max}$ is shown.

Mass	**Z**	**[Fe/H]**	**Ev Phase**	**EEP**	**Age**	n	$\nu_{\mathtt{test}}$	$\varepsilon_{\mathtt{dmesh}}$	$\%\varepsilon_{\mathtt{dmesh}}$
$M_\odot$		dex			Myr		cyc/day	cyc/day	$\varepsilon_{\mathtt{dmesh}}/\nu_{\mathrm{test}}$
Model Class 3: metal-poor, solar mass									
1.0	0.0017	-1.0	MS	187	2570.72	5	66.9	0.11	0.16
1.0	0.0017	-1.0	subgiant	303	5507.88	5	36.0	0.04	0.10
Model Class 4: very metal-poor, solar mass									
1.0	0.0002	-2.0	MS	187	1963.00	5	73.7	0.17	0.24
1.0	0.0002	-2.0	subgiant	303	5166.21	5	38.7	0.04	0.10
Model Class 5: solar metallicity, $1.4M_\odot$									
1.4	0.0162	0.0	MS	187	1462.16	5	40.7	0.18	0.44
1.4	0.0162	0.0	subgiant	303	2356.83	5	30.3	0.06	0.18
Model Class 6: solar metallicity, $2.5M_\odot$									
2.5	0.0162	0.0	MS	187	321.41	5	26.0	0.23	0.88
2.5	0.0162	0.0	subgiant	303	470.04	5	15.5	0.25	1.64
Model Class 7: solar metallicity, $5.0M_\odot$									
5.0	0.0162	0.0	MS	187	57.39	5	19.5	0.07	0.36
5.0	0.0162	0.0	subgiant	303	80.77	5	11.0	0.10	0.92

Table 4. Frequency discrepancies due to structural resolution, $\varepsilon_{\mathtt{dmesh}}$, calculated for upper main-sequence pulsators (including δ Scutis). $\varepsilon_{\mathtt{dmesh}}$ is evaluated for $n = 3$, $\ell = 0$ modes. Note that age is shown in Myr instead of Gyr.

Mass	**Z**	**[Fe/H]**	**Ev Phase**	**EEP**	**Age**	n	$P_{\mathtt{test}}$	$\zeta_{\mathtt{dmesh}}$	$\%\ \zeta_{\mathtt{dmesh}}$
$M_\odot$		dex			Gyr	$\ell, m = 0$	days		$\zeta_{\mathtt{dmesh}}/P_{\mathrm{test}}$
Model Class 1: Solar-like									
1.0	0.0162	0.0	AGB	1198	10.50	1	98.26	20.93	21.27
Model Class 2: metal-rich, solar mass									
1.0	0.0447	+0.5	AGB	1198	11.44	1	390.16	7.91	2.03
Model Class 3: metal-poor, solar mass									
1.0	0.0017	-1.0	AGB	1198	6.38	1	37.49	3.69	9.85
Model Class 4: very metal-poor, solar mass									
1.0	0.0002	-2.0	AGB	1198	5.73	1	23.72	0.12	0.50
Model Class 5: solar metallicity, $1.4M_\odot$									
1.4	0.0162	0.0	AGB	1198	3.22	1	77.87	8.59	10.98
Model Class 6: solar metallicity, $2.5M_\odot$									
2.5	0.0162	0.0	AGB	1198	0.68	1	33.95	2.82	8.29
Model Class 7: solar metallicity, $5.0M_\odot$									
5.0	0.0162	0.0	AGB	1198	0.10	1	200.79	1.09	0.54

Table 5. Period discrepancies due to structural resolution, $\zeta_{\mathtt{dmesh}}$, calculated for Mira variables. $\zeta_{\mathtt{dmesh}}$ is evaluated at the fundamental mode frequency, $n = 1, \ell = 0, m = 0$.

3. RESOLUTION UNCERTAINTY CALCULATIONS

We present calculations of the resolution uncertainty term for solar-like, upper main-sequence, and Mira oscillators in Tables 3, 4, and 5, respectively, for the set of reference EEPs representing different evolutionary phases introduced in Section 2. Tables 3 and 4 provide the frequency-based resolution uncertainty term $\varepsilon_{\mathtt{dmesh}}$ (equation 3), whereas Table 5 presents the analogous quantity, $\zeta_{\mathtt{dmesh}}$, in period (equation 5).

Table 3 shows $\varepsilon_{\mathtt{dmesh}}$ calculations for solar-like oscillators, whose pressure modes are driven by stochastic excitation in the surface convection zone. The most useful and likely-to-be-observed p-mode in this case is the one closest to ν_{max}, the frequency of maximum power. As ν_{max} changes depending on the properties of the solar-like oscillator, so does our test frequency. Table 3 thus provides the radial orders n of the two modes bracketing ν_{max} along with ν_{max}, $\varepsilon_{\mathtt{dmesh}}$, and the quantity

$\varepsilon_{\texttt{dmesh}}/\nu_{\max}$, in μHz. The lattermost of these quantities indicates the fractional uncertainty.

Table 4 shows the same for upper main-sequence oscillators, but the test frequency in these cases is the one corresponding to a fixed mode of radial order $n = 3$ $(\ell, m = 0)$. This was chosen because δ Scutis typically pulsate in low-order p modes, although the precise mode selection process remains somewhat uncertain (Dupret et al. 2005; Xiong et al. 2016). Frequencies are reported here in cycles per day.

Lastly, Table 5 presents the resolution-induced discrepancy in terms of period, in days, for Miras, using a test period $P_{\rm test}$ fixed to $n = 1$ $(\ell, m = 0)$ and the absolute period discrepancy $\zeta_{\texttt{dmesh}}$. Pressure variations in this regime are driven by the κ-mechanism in the He II ionization zone. The most appropriate test value here is the period corresponding to the fundamental pressure mode, or FM, as this is the mode overwhelmingly likely to correspond to the dominant periodicity observed in these stars (Soszyński et al. 2013; Trabucchi et al. 2017; Molnár et al. 2019; Trabucchi et al. 2021; Joyce et al. 2024).

Figure 3 shows the evolution of the fractional uncertainty term across the HRD. Panels in the left-hand column show tracks with the same metallicity and different masses; panels in the right-hand column show tracks with the same mass and different metallicities. Panels in the top row highlight solar-like oscillators, panels in the middle row show upper main-sequence oscillators, and panels in the bottom row show Miras.

Notable features and trends revealed by Tables 3, 4 and 5 and Figure 3 include:

- resolution-based uncertainty contributions $\varepsilon_{\texttt{dmesh}}/\nu$ and $\zeta_{\texttt{dmesh}}/P$ are larger for higher-mass models and higher-metallicity models;

- $\varepsilon_{\texttt{dmesh}}/\nu$ and $\zeta_{\texttt{dmesh}}/P$ generally increase as evolutionary stage increases, with the AGB/Mira regions hosting contributions near the 3% level;

- fractional uncertainties for solar-like oscillators are below 1% for models $\leq 1.4 M_\odot$; and

- AGB models show the largest variance in $\zeta_{\texttt{dmesh}}/P$—between 0.5 to 20%—across mass and metallicity and the largest absolute error contribution, with $\zeta_{\texttt{dmesh}}/P_{\rm test}$ near or exceeding 10% in four of the seven model classes.

While it is generally well-established that modeling uncertainties of all types become larger the further the model deviates from solar parameters (Joyce & Chaboyer 2018a; Tayar et al. 2022; Cinquegrana et al. 2022; Joyce et al. 2023; Cinquegrana et al. 2023), these calculations provide quantitative benchmarks as a function of evolutionary phase for the (un-)reliability of stellar models computing with `MESA`'s default resolution setting.

4. COMPARISON TO *TESS* OBSERVATIONAL UNCERTAINTIES

With % $\varepsilon_{\texttt{dmesh}}$ and % $\zeta_{\texttt{dmesh}}$ falling below the 1% level for the majority of models, it is reasonable to ask how important such considerations are in the context of other sources of uncertainty in the asteroseismic parameter determination process. To answer this question, it is most informative to compare the mesh resolution uncertainties calculated above to typical observational uncertainties as a function of stellar type. This section uses TESS (Ricker et al. 2015) as the example instrument, though these calculations can be easily translated to Kepler (Borucki et al. 2010), and the method can be generalized to any instrument.

4.1. *Simulating Observational Uncertainties*

We now simulate the typical uncertainty for observed oscillation modes of the types studied here (solar-like, δ Scuti, and Mira) using the noise characteristics of the TESS instrument.

To represent realistic observational scenarios, we select two noise values corresponding to 5th and 10th magnitude stars. Assuming a nominal 2 min cadence, the per-cadence noise $\sigma_{\rm noise/cadence}$ is determined using the ATL calculator provided by Hey et al. (2024)[2]. Regardless of the chosen cadence, the time-domain scatter $\sigma_{\rm noise}$ is approximately 19 ppm$\cdot$hr^{-1} and 197 ppm$\cdot$hr^{-1}, respectively. These values, without loss of generality, are comparable to those for 10th and 15th magnitude stars observed by Kepler (Gilliland et al. 2011).

We simulate mode amplitudes based on stellar parameters. For solar-like oscillators, we adopt established scaling relations for predicting asteroseismic detection yields:

$$A_{\rm osc} = \frac{(L/{\rm L}_\odot)^{0.84}\beta}{(M/{\rm M}_\odot)^{1.32}(T_{\rm eff}/{\rm K})c_k} \times 22167.48 \text{ ppm}, \quad (6)$$

where $c_k = (T_{\rm eff}/5934 \text{ K})^{0.8}$ (Huber et al. 2011; Chaplin et al. 2011; Campante et al. 2016; Schofield et al. 2019). The factor β accounts for amplitude suppression for stars near the δ Sct instability strip,

$$\beta = 1 - \exp((T_{\rm eff} - T_{\rm red}(L/{\rm L}_\odot)^{0.093})/1550 \text{ K}) \quad (7)$$

[2] https://github.com/danhey/tess-atl

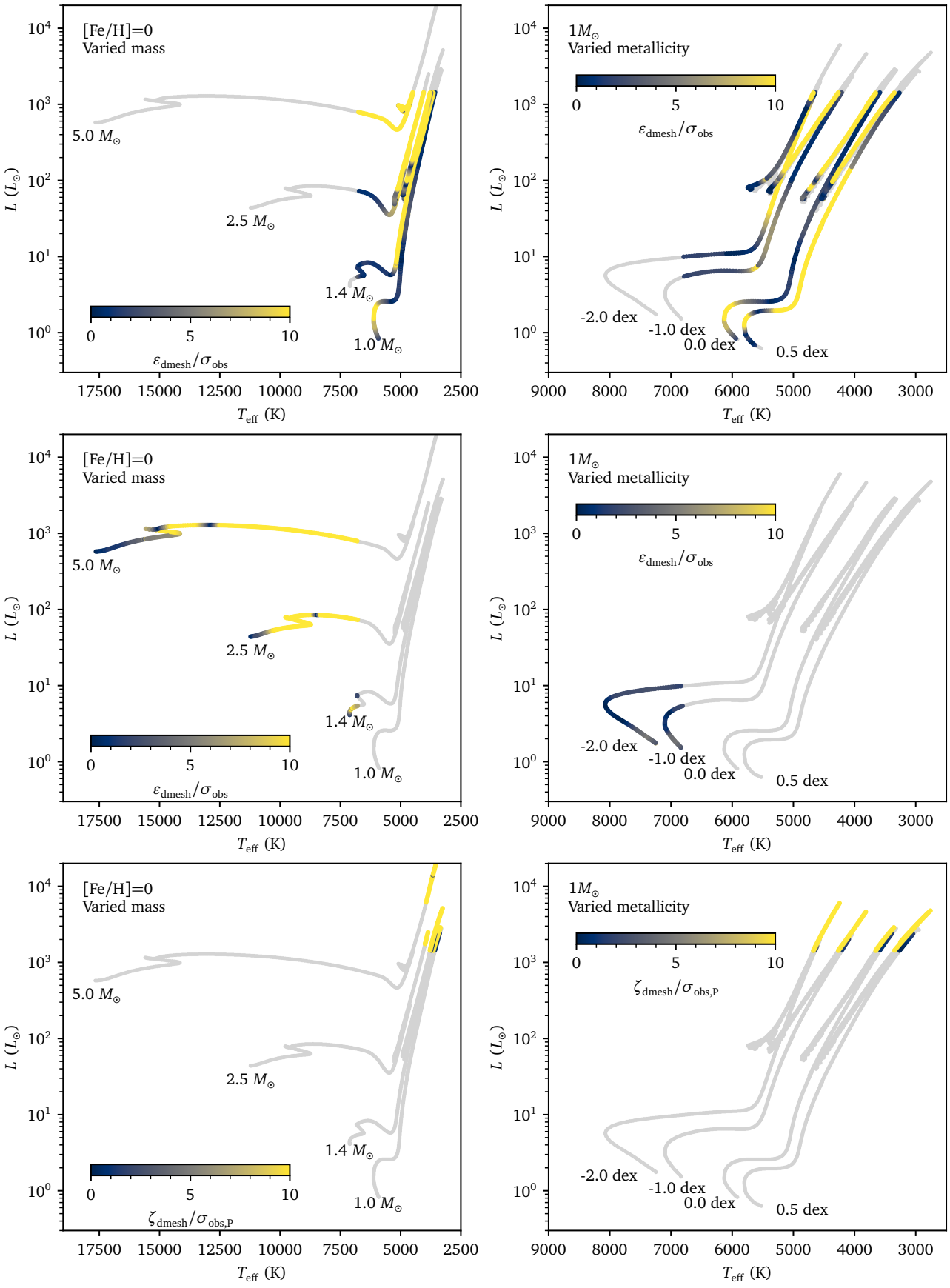

Figure 4. H–R diagram color-coded by the ratio of $\varepsilon_{\texttt{dmesh}}$ ($\zeta_{\texttt{dmesh}}$) to the typical observational uncertainties $\sigma_{\rm obs}$ (or $\sigma_{\rm obs,\,P}$), assuming the worst-case observing scenario (T=1 month, $\sigma_{\rm noise}$ = 197 ppm/hr). The left panel shows all models with solar metallicity but different masses, and the right panel with solar mass but different metallicites.

mass	**[Fe/H]**	**Phase**	$\varepsilon_{\texttt{dmesh}}$	$\varepsilon_{\texttt{dmesh}}/\sigma_{\textbf{obs}}$	$\varepsilon_{\texttt{dmesh}}/\sigma_{\textbf{obs}}$	$\varepsilon_{\texttt{dmesh}}/\sigma_{\textbf{obs}}$	$\varepsilon_{\texttt{dmesh}}/\sigma_{\textbf{obs}}$	$\varepsilon_{\texttt{dmesh}}/\sigma_{\textbf{obs}}$	$\varepsilon_{\texttt{dmesh}}/\sigma_{\textbf{obs}}$
			μHz	T=4 yrs	T=1 yrs	T=0.083 yrs	T=4 yrs	T=1 yrs	T=0.083 yrs
				$\sigma_{\rm noise}$=19.1	$\sigma_{\rm noise}$=19.1	$\sigma_{\rm noise}$=19.1	$\sigma_{\rm noise}$=197	$\sigma_{\rm noise}$=197	$\sigma_{\rm noise}$=197
Model Class 1: Solar-like									
1.0	0.0	MS	11.950	562	281	74.7	54.6	27.3	7.3
1.0	0.0	subgiant	11.331	1018	509	133	99.0	49.5	13.0
1.0	0.0	early RGB	0.339	77.3	38.6	9.1	7.5	3.8	0.9
1.0	0.0	late RGB	0.001	1385	243	6.0	135	23.6	0.6
1.0	0.0	CHeB	0.061	429	213	35.4	41.7	20.7	3.4
Model Class 2: metal-rich, solar mass									
1.0	+0.5	MS	2.843	139	69.3	18.0	13.5	6.7	1.7
1.0	+0.5	subgiant	12.939	1133	566	145	110	55.0	14.1
1.0	+0.5	early RGB	9.228	1815	906	209	176	88.0	20.3
1.0	+0.5	late RGB	0.003	8734	1172	28.2	848	114	2.7
1.0	+0.5	CHeB	0.009	172	82.9	6.8	16.7	8.0	0.7
Model Class 3: metal-poor, solar mass									
1.0	-1.0	early RGB	2.040	267	134	37.8	26.0	13.0	3.7
1.0	-1.0	late RGB	0.001	656	292	14.7	63.7	28.4	1.4
1.0	-1.0	CHeB	0.008	12.4	6.2	1.7	1.2	0.6	0.2
Model Class 4: very metal-poor, solar mass									
1.0	-2.0	early RGB	0.756	191	95.4	26.9	18.5	9.3	2.6
1.0	-2.0	late RGB	0.008	1674	825	103	163	80.1	10.0
1.0	-2.0	CHeB	0.048	34.0	17.0	4.8	3.3	1.7	0.5
Model Class 5: solar metallicity, $1.4M_\odot$									
1.4	0.0	subgiant	0.495	51.0	25.5	6.9	5.0	2.5	0.7
1.4	0.0	early RGB	0.059	14.9	7.5	1.8	1.5	0.7	0.2
1.4	0.0	late RGB	0.007	16758	3741	96.7	1627	363	9.4
1.4	0.0	CHeB	0.031	127	63.1	11.8	12.3	6.1	1.1
Model Class 6: solar metallicity, $2.5M_\odot$									
2.5	0.0	early RGB	1.608	554	277	74.4	53.8	26.9	7.2
2.5	0.0	late RGB	0.137	3232	1592	197	314	155	19.1
2.5	0.0	CHeB	1.086	637	318	83.4	61.9	30.9	8.1
Model Class 7: solar metallicity, $5.0M_\odot$									
5.0	0.0	early RGB	0.276	21465	10662	1770	2085	1036	172
5.0	0.0	late RGB	0.185	84509	40971	3695	8208	3979	359
5.0	0.0	CHeB	0.007	746	371	70.1	72.5	36.1	6.8

Table 6. Comparison of resolution-induced numerical vs observational uncertainties for solar-like (p-mode) oscillators. The observational uncertainties are evaluated for six different combinations of observing strategies, defined by three observing durations (T = 1 month, 1 year, and 4 years) and two noise levels ($\sigma_{\rm noise}$ = 19.1 ppm/hr and 197 ppm/hr), which corresponds to 5th and 10th magnitude TESS stars or 10th and 15th magnitude Kepler stars. We estimate stellar oscillation amplitudes based on their stellar properties, including mass, luminosity, and $T_{\rm eff}$.

mass	[Fe/H]	Phase	$\varepsilon_{\rm dmesh}$	$\varepsilon_{\rm dmesh}/\sigma_{\rm obs}$	$\varepsilon_{\rm dmesh}/\sigma_{\rm obs}$	$\varepsilon_{\rm dmesh}/\sigma_{\rm obs}$	$\varepsilon_{\rm dmesh}/\sigma_{\rm obs}$	$\varepsilon_{\rm dmesh}/\sigma_{\rm obs}$	$\varepsilon_{\rm dmesh}/\sigma_{\rm obs}$
			cyc/day	T=4 yrs $\sigma_{\rm noise}$=19.1	T=1 yrs $\sigma_{\rm noise}$=19.1	T=0.083 yrs $\sigma_{\rm noise}$=19.1	T=4 yrs $\sigma_{\rm noise}$=197	T=1 yrs $\sigma_{\rm noise}$=197	T=0.083 yrs $\sigma_{\rm noise}$=197
Model Class 3: metal-poor, solar mass									
1.0	-1.0	MS	0.11	28060	3508	83.9	2729	341	8.2
1.0	-1.0	subgiant	0.04	9167	1146	27.4	891	111	2.7
Model Class 4: very metal-poor, solar mass									
1.0	-2.0	MS	0.17	44228	5529	132	4302	538	12.9
1.0	-2.0	subgiant	0.04	10332	1291	30.9	1005	126	3.0
Model Class 5: solar metallicity, $1.4M_\odot$									
1.4	0.0	MS	0.18	46685	5836	140	4540	567	13.6
1.4	0.0	subgiant	0.06	14332	1792	42.8	1394	174	4.2
Model Class 6: solar metallicity, $2.5M_\odot$									
2.5	0.0	MS	0.23	60593	7574	181	5900	738	17.6
2.5	0.0	subgiant	0.25	66767	8346	200	6499	812	19.4
Model Class 7: solar metallicity, $5.0M_\odot$									
5.0	0.0	MS	0.07	19273	2409	57.6	1881	235	5.6
5.0	0.0	subgiant	0.10	27667	3458	82.7	2699	337	8.1

Table 7. Same as Table 6, but for upper main-sequence pulsators (including δ Scutis). We adopt a minimum amplitude estimate of 14 ppm for all cases.

mass	[Fe/H]	Phase	$dP_{\rm dmesh}$	$\zeta_{\rm dmesh}/\sigma_{{\rm obs},P}$	$\zeta_{\rm dmesh}/\sigma_{{\rm obs},P}$	$\zeta_{\rm dmesh}/\sigma_{{\rm obs},P}$	$\zeta_{\rm dmesh}/\sigma_{{\rm obs},P}$	$\zeta_{\rm dmesh}/\sigma_{{\rm obs},P}$	$\zeta_{\rm dmesh}/\sigma_{{\rm obs},P}$
			days	T=4 yrs $\sigma_{\rm noise}$=19.1	T=1 yrs $\sigma_{\rm noise}$=19.1	T=0.083 yrs $\sigma_{\rm noise}$=19.1	T=4 yrs $\sigma_{\rm noise}$=197	T=1 yrs $\sigma_{\rm noise}$=197	T=0.083 yrs $\sigma_{\rm noise}$=197
Model Class 1: Solar-like									
1.0	0.0	AGB	98.3	706814	92178	2211	68612	8948	215
Model Class 2: metal-rich, solar mass									
1.0	+0.5	AGB	390.2	67360	8422	201	6537	817	19.5
Model Class 3: metal-poor, solar mass									
1.0	-1.0	AGB	37.5	111740	41564	1435	10851	4036	139
Model Class 4: very metal-poor, solar mass									
1.0	-2.0	AGB	23.7	1749	853	84.3	170	82.8	8.2
Model Class 5: solar metallicity, $1.4M_\odot$									
1.4	0.0	AGB	77.9	594488	81308	1957	57712	7893	190
Model Class 6: solar metallicity, $2.5M_\odot$									
2.5	0.0	AGB	33.9	350091	80791	2107	33993	7845	205
Model Class 7: solar metallicity, $5.0M_\odot$									
5.0	0.0	AGB	200.8	1641233	225344	5426	159329	21876	527

Table 8. Same as Table 6, but for Miras. We estimate oscillation amplitudes based on the fitted luminosity-amplitude relation (Equation 8).

(Schofield et al. 2019; Hey et al. 2024). For upper main-sequence pulsators, we adopt a conservative value of $A_{\rm osc} = 14$ ppm, reflecting the typical range of δ Sct oscillation amplitudes, which span from 14 to 30000 ppm (Aerts et al. 2010).

For Mira variables, we applied an amplitude–luminosity relation calculated based on the high-luminosity variable catalog of Yu et al. (2020):

$$\log(A_{\rm osc}/{\rm ppm}) = -0.82\log(L/{\rm L}_\odot) + 0.45\log(L/{\rm L}_\odot)^2 + 2.00. \quad (8)$$

Next, we calculate mode lifetimes. Solar-like oscillations have finite lifetimes τ, which are related to mode linewidths Γ through $\tau = 1/(\pi\Gamma)$. Mode linewidths are

determined using the fit equation:

$$\log(\Gamma/\Gamma_0) = c_1 \log(T_{\rm eff}/5777\ {\rm K}) + c_2 \log(g/274\ {\rm m\cdot s^{-1}}), \quad (9)$$

where Γ_0, c_1, and c_2 are coefficients provided in Table 5 of Li et al. (2020). We adopt separate parameterizations for main-sequence (MS) and red giant branch (RGB) stars, with a $\log g$ cutoff of 3.5 distinguishing the two regimes. For δ Sct and Mira-like variables, the modes were treated as coherent with effectively infinite lifetimes.

Based on these noise properties, mode amplitudes, and mode lifetimes, we estimate the expected uncertainties of mode frequencies as in Kjeldsen & Bedding (2012):

$$\sigma_{\rm obs} \approx 0.44\sqrt{\pi/N}\sigma_{\rm noise/cadence}A_{\rm osc}^{-1}\sqrt{T^{-2}+\tau^{-2}}, \quad (10)$$

where T is the total observing time and N is the number of data points in the time series. In period, this becomes

$$\sigma_{{\rm obs},P} = \frac{\sigma_{\rm obs}}{\nu_{\rm test}^2}. \quad (11)$$

We consider three typical values for the total observing time T: 4 years, 1 year, and one month (0.0833 years).

4.2. *Ratio Between Numerical And Observational Uncertainties*

Tables 6 (solar-like), 7 (upper main-sequence), and 8 (Miras) compare resolution-based numerical uncertainty to observational uncertainty for six different combinations of observing strategies, defined by three observing durations (T = 1 month, 1 year, and 4 years) and two noise levels ($\sigma_{\rm noise}$ = 19.1 ppm/hr and 197 ppm/hr), which corresponds to 5th and 10th magnitude TESS stars or 10th and 15th magnitude Kepler stars. The ratio $\varepsilon_{\texttt{dmesh}}/\sigma_{\rm obs}$ (or $\zeta_{\texttt{dmesh}}/\sigma_{\rm obs,\,P}$) provides a measure of the numerical uncertainty induced by mesh resolution relative to observational noise. As in Tables 3, 4 and 5, measurements are taken at preferred EEPs representative of different stellar evolutionary phases.

When assuming the best-case observing scenario, with a 4-year observing time and a noise level of 19.1 ppm/hr, we find that resolution-based numerical uncertainties are consistently orders of magnitude larger than the observational uncertainties, regardless of evolutionary phase or stellar type. The situation is least dire for solar-like oscillators, whose resolution-based uncertainties dominate over observational uncertainties by a factor of a few hundred; upper main-sequence models are 10 to 100x worse than this, and Miras are another factor of ten worse than δ Scutis.

Following Figure 3, we compute the observational uncertainty $\sigma_{\rm obs}$ under the assumptions of the worst-case observing scenario (T = 0.038 yr, $\sigma_{\rm obs}$ = 197) and evaluate the ratio of $\varepsilon_{\texttt{dmesh}}$ to $\sigma_{\rm obs}$ (or $\zeta_{\texttt{dmesh}}$ to $\sigma_{\rm obs,\,P}$) along the entire evolutionary tracks representing each model class. The worst-case observing scenario produces mesh-to-observational uncertainty ratios of order unity for most solar-like oscillators, indicating that $\varepsilon_{\texttt{dmesh}}$ is comparable to the observational uncertainty in this scenario. As expected per the calculations in Section 3, these ratios are worse for higher-mass stars and later evolutionary stages. Ratios for δ Scutis are comparable to those for solar-like oscillators under worst-case observing assumptions, and ratios for Miras are about a factor of 10 worse.

It is worth noting that in the case of Mira variables, the observational uncertainty as we have computed here—based primarily on instrumentation—is very unlikely to be among the dominant sources of uncertainty in characterizing them observationally. Miras are notoriously difficult to constrain observationally due issues such as meandering, period decay, and large-amplitude brightness variations, all of which can shift the values of their fundamental parameters significantly over relatively short periods of time (Kiss et al. 2006; Bányai et al. 2013; Molnár et al. 2019; Merchan-Benitez et al. 2023). As many studies have shown, modeling such stars is similarly complicated (e.g. Karakas 2011), and for that reason, proper AGB modeling demands very high structural resolution and treatment of non-adiabatic effects (e.g. Zinn et al. 2023; Joyce et al. 2024). While we do not incorporate non-adiabatic effects, mass loss, or other considerations necessary for proper AGB modeling here, the extreme values of $\zeta_{\texttt{dmesh}}/\sigma_{\rm obs,\,P}$ in Table 8 nonetheless provide a representative portrait of the extent to which modeling uncertainty obliterates instrumental noise for late-stage, high-amplitude variable stars.

5. IMPLICATIONS FOR MODERN ASTEROSEISMIC TECHNIQUES

One of the key powers of asteroseismology is its ability to provide constraints on the sub-surface properties of stars. This enables far more precise determinations of the fundamental stellar parameters that are closely tied to the physics of stellar interiors, such as mass and age, than can be obtained using classical observational techniques alone.

So far, we have quantified the impact of mesh uncertainty on individual p-mode frequencies. While valuable in their own right, these frequencies are, more importantly, essential ingredients in a number of modern as-

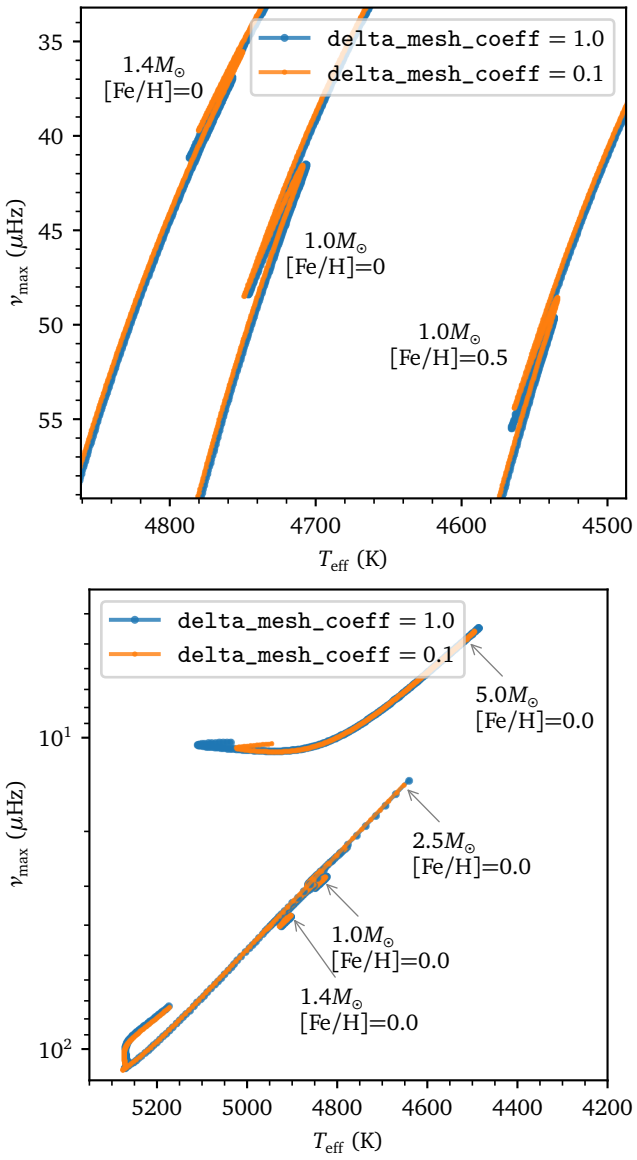

Figure 5. Seimic H–R diagram (ν_{max} vs. T_{eff}) around the RGB bump (top panel) and the CHeB phase (bottom panel).

teroseismic techniques ranging from period-spacing diagrams to age determination methods. We now discuss the potential impacts of improper treatment of structural resolution in the context of these techniques. We begin with the most direct inferences based on p-modes and conclude with the most derived.

5.1. *Evolutionary Features on the H–R Diagram*

The red giant branch bump, or RGBB, is an evolutionary feature that occurs in stars with surface convective envelopes. During this phase, the star's luminosity temporarily drops along the RGB as a result of the encounter between the outwardly expanding hydrogen-burning shell and the chemical discontinuity left by the receding convective envelope (Joyce & Chaboyer 2015; Christensen-Dalsgaard 2015; Tayar & Joyce 2022). Because the RGBB is a direct probe of the maximum depth of penetration of the convective envelope (e.g. Fraser et al. 2022), convective overshoot in the envelope reduces the luminosity, or increases the oscillation frequency, ν_{max}, at which the bump occurs. This makes p-modes a sensitive probe of the physics of envelope overshoot (Angelou et al. 2015; Khan et al. 2018).

The upper panel of Figure 5 illustrates the impact of $\varepsilon_{\texttt{dmesh}}$ on the location of the RGBB in the ν_{max}-T_{eff} plane for tracks with convective envelopes. The median fractional uncertainty of ν_{max} is 0.6% (Pinsonneault et al. 2024), yet we observe differences of approximately 2% in the locations of the maximal and minimal luminosities of the bump due to differences in $\varepsilon_{\texttt{dmesh}}$. The resolution-induced uncertainty therefore dominates over the fractional uncertainty of ν_{max} by more than a factor of three.

The locations of core helium burning (CHeB) and the horizontal branch (red clump) more broadly are influenced by core overshoot, both during the main sequence (i.e. relic effects) and during the clump phase, and are therefore also sensitive to mesh resolution. Figure 5 demonstrates the influence of `delta_mesh_coeff` on evolutionary tracks of varying mass in the ν_{max}–T_{eff} diagram. The agreement for high-mass tracks is poorer, with temperature differences reaching up to 100 K. Additionally, morphological variations are evident, stemming from different resolution treatments, especially near the convective core boundary.

Under-resolving the stellar profile will always impact a model's evolution to some degree, but it is especially dangerous around boundary regions. For example, the Schwarzschild or Ledoux criterion for stability against convection is evaluated at every mesh point in a stellar model, and this determines the location, size, and persistence of convective and radiative zones.

The development of convection zones in models is sensitive to resolution, and whether a model star develops a convective core on the main sequence significantly impacts its subsequent evolution. Similarly, any model that hosts a complicated interior structure, such as the double-shell burning in AGB stars, will be particularly sensitive to mesh resolution. Modeling AGB stars requires adequately resolving multiple boundaries, and the number and duration of thermal pulses an AGB model undergoes is well known to be sensitive to the number of grid points used in the interior (Cinquegrana et al. 2023; Joyce et al. 2024).

5.2. *Seismic Parameters: Period Spacings, Frequency Ratios, and Phase Offset*

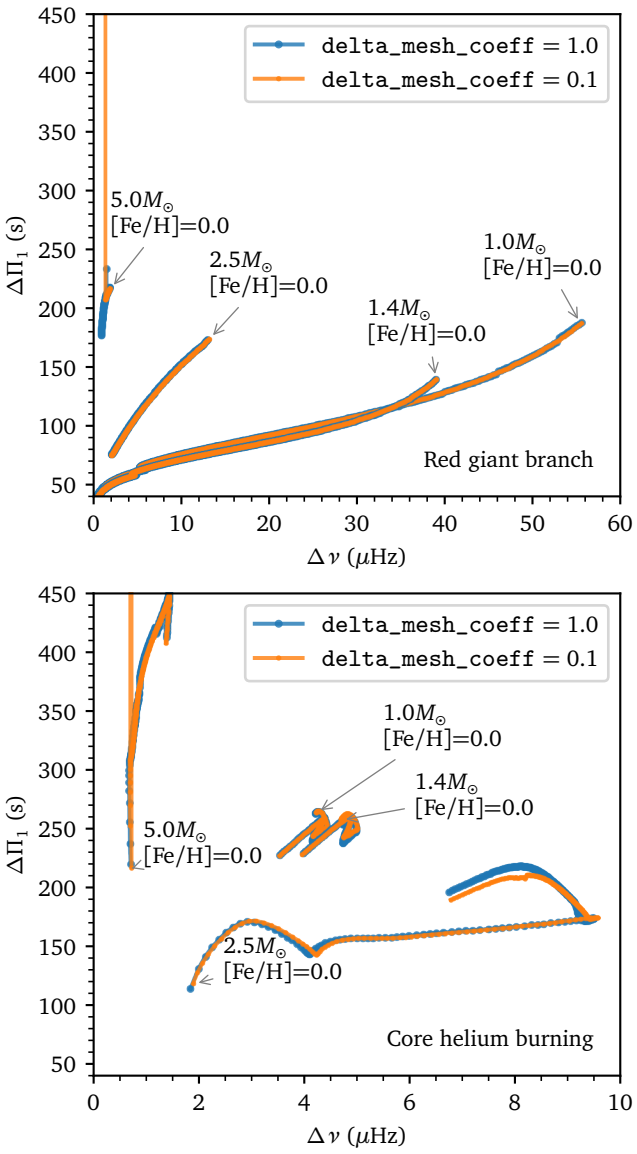

Figure 6. Seismic $\Delta\Pi_1$–$\Delta\nu$ diagram for RGB (top panel) CHeB phase (bottom panel).

In Section 3, we analyzed the frequency response to `delta_mesh_coeff` as a function of evolutionary phase (EEP). However, evolutionary stage is not directly measurable through observation. Instead, seismic observables, such as the p-mode frequency separation ($\Delta\nu$), g-mode period spacing ($\Delta\Pi_1$), frequency ratios (r_{02} and r_{13}), and the p-mode phase offset (ϵ_p) are more commonly compared to predictions from stellar models. We should therefore assess the impact of `delta_mesh_coeff` in terms of these seismic observables. In this analysis, we focus on the variation of seismic parameters as a function of the large frequency separation, $\Delta\nu$, calculated from linearly fitting radial mode frequencies $\nu_{n,\ell=0}$ as a function of radial order n:

$$\nu_{n,\ell=0} = \Delta\nu(n + \epsilon_p). \tag{12}$$

The g-mode period spacing is given by

$$\Delta\Pi_l = \frac{2\pi^2}{\sqrt{l(l+1)}} \left(\int \frac{N}{r} \mathrm{d}r \right)^{-1}, \tag{13}$$

where N is the buoyancy frequency. This quantity probes the inner cavity of the near-core, radiative region in which g modes propagate (Pedersen et al. 2021; Noll et al. 2024). Figure 6 compares the evolution of $\Delta\Pi_1$ as a function of $\Delta\nu$ for tracks with different resolutions. The upper panel highlights the red giant region, and the lower panel highlights the core helium-burning region. In both regions, higher-mass models show the largest discrepancy (i.e. poorest convergence). This is because $\Delta\Pi_1$ is measured from the convective core boundary, which will be improperly resolved with low mesh sampling. The typical uncertainty in observational measurements of $\Delta\Pi_1$ is below 1 s (Vrard et al. 2016; Gehan et al. 2018; Kuszlewicz et al. 2023; Li et al. 2024a; Hatt et al. 2024). While the change in $\Delta\Pi_1$ as a function of `delta_mesh_coeff` is below this threshold for the 1.0 and 1.4$M_\odot$ tracks in both the red giant and core helium-burning regions, the resolution-based discrepancy for the higher-mass (2.5, 5.0$M_\odot$) tracks ranges from 2-10 seconds.

For low-mass and solar-like main-sequence stars, seismic frequency spacing ratios such as r_{02} and r_{13} can be used to estimate stellar ages (e.g. Joyce & Chaboyer 2018b) because they are sensitive to the near-core composition (Christensen-Dalsgaard 1984; Roxburgh & Vorontsov 2003). Likewise, the p-mode phase term, ϵ_p, aids in mode identification (e.g., in F stars and δ Scuti stars; White et al. 2011; Murphy et al. 2021) and can probe the acoustic depths of the HeII ionization zone and the bottom of the outer convection zone (Broomhall et al. 2014; Verma et al. 2019; Dréau et al. 2020). We calculated frequency ratios following the definitions of Roxburgh & Vorontsov (2003) and averaged across radial orders, and calculated ϵ_p following Equation 12. Figures 7 and 8 present frequency ratios and ϵ_p, respectively, as a function of $\Delta\nu$ for solar-mass tracks. Per the residuals in the lower panels of these Figures, differences are minimal when these three quantities are evaluated at the same $\Delta\nu$ but different `delta_mesh_coeff`. Hence, these quantities are robust against resolution uncertainty.

It is important to recognize that `delta_mesh_coeff` influences both $\Delta\nu$ and the seismic quantities discussed above in a correlated manner. Hence, structural changes in the star induced by `delta_mesh_coeff` will propagate through all mode frequencies and therefore all of these quantities, leading to interdependent variations. As a

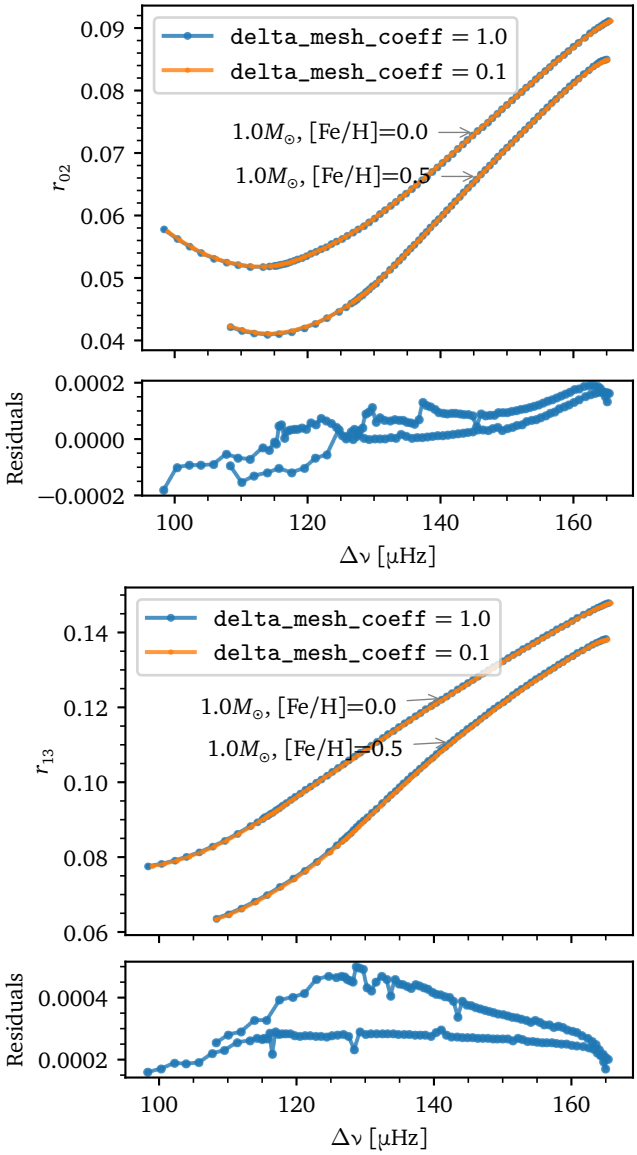

Figure 7. Seismic ratios (r_{01} and r_{13}) vs. $\Delta\nu$ for low-mass main-sequence models. The bottom panels show the residuals between the two `delta_mesh_coeff` tracks.

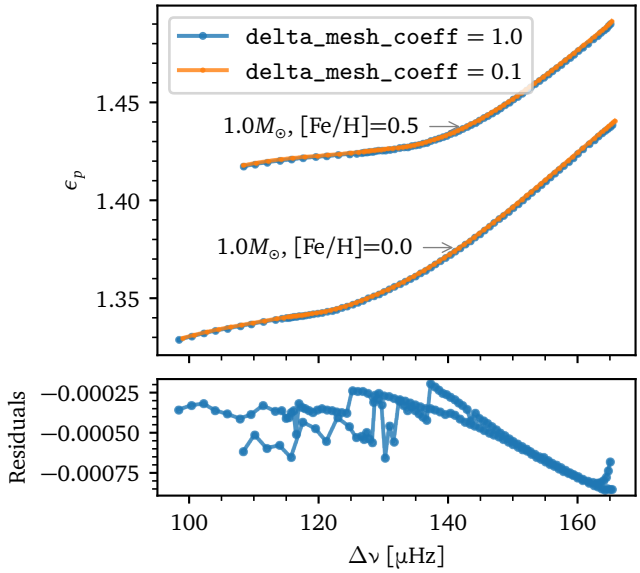

Figure 8. P-mode phase offset ϵ_p vs. $\Delta\nu$ for low-mass main-sequence models. The bottom panels show the residuals between the two `delta_mesh_coeff` tracks.

result, the projections of these variations along seismic axes ($\Delta\nu$) may make discrepancies appear smaller than they actually are as a function of evolutionary stage (i.e. in EEP space).

Though we do not investigate this issue explicitly here, it is further worth noting that mixed modes, being the result of coupling between p and g modes, will be affected by p mode uncertainties as well.

5.3. *Effect on Stellar Mass, Radius, Age, and Density*

We now estimate the influence of `delta_mesh_coeff` on individual mode frequencies and the associated impact on deriving classical stellar parameters, including mass, radius and age. Additionally, we examine the model-based $f_{\Delta\nu}$ factor, which is used to relate the $\Delta\nu$ to the stellar mean density through (Sharma et al. 2016)

$$\frac{\Delta\nu}{135.1\ \mu\text{Hz}} = f_{\Delta\nu}\left(\frac{\rho}{\rho_\odot}\right)^{0.5}. \tag{14}$$

For this exercise, we chose a mode near the test frequency appropriate for each case (see Tables 3, 4 and 5) and determined interpolated values for radius, age, and $f_{\Delta\nu}$ as functions of that mode frequency for two evolutionary tracks with different `delta_mesh_coeff` values. Because mode frequencies are not strictly monotonic with evolution, we focus on only a few segments of the tracks where monotonicity is satisfied. We then computed differences in radius, age, and $f_{\Delta\nu}$ at the same frequency. Figure 9 presents the fractional differences in radius and age, along with the absolute differences in $f_{\Delta\nu}$, as a function of evolutionary stage.

Asteroseismic constraints can achieve uncertainties of approximately 2% in radius, 4% in mass, and 10% in age for red giants (Montalbán et al. 2021; Li et al. 2022b; Pinsonneault et al. 2024) and cool main-sequence dwarfs (Silva Aguirre et al. 2015, 2017) in optimal conditions. These uncertainties can be even lower for δ Scuti stars (Murphy et al. 2021). Determining these parameters for AGB stars is difficult, but Miras with two modes identified have been constrained to within 8% in mass and 20% in age (Molnár et al. 2019).

Figure 9 therefore shows that, for early main-sequence dwarfs, age uncertainties induced by `delta_mesh_coeff` appear to approach the level of observational uncer-

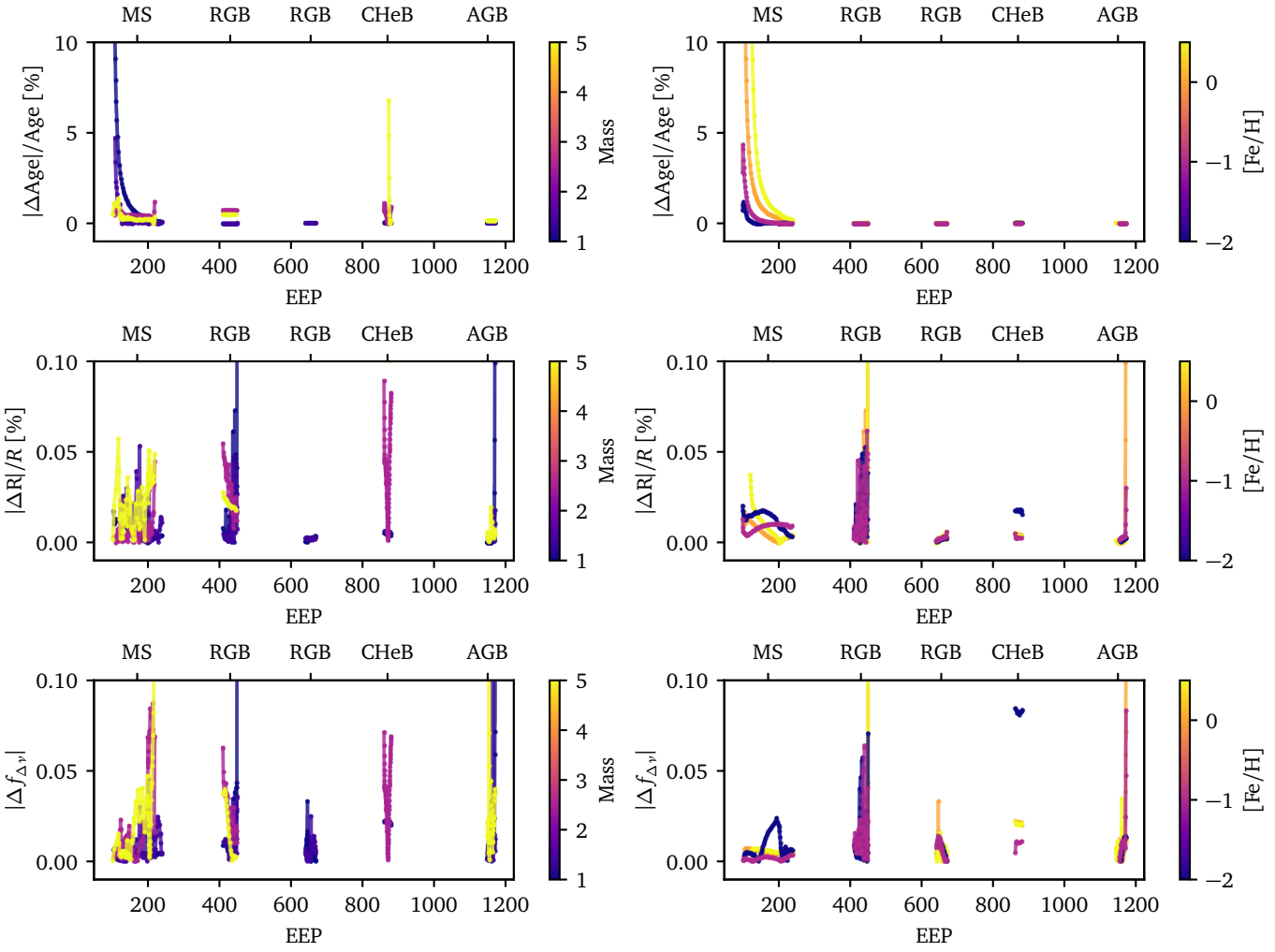

Figure 9. Differences in stellar parameters (Age, R, and $f_{\Delta\nu}$, from top row to bottom row, respectively) when evaluated against the same oscillation frequency for the two tracks with different `delta_mesh_coeff`. The left columns show tracks with varying mass, and the right columns show those with varying metallicity.

tainty. As stars evolve, their total ages increase while fractional age uncertainties decrease, reducing the relative impact of `delta_mesh_coeff` on age estimation in later stages of evolution. Given the approximate scaling of stellar mass with age via $M \sim \tau^{-1/4}$, the uncertainties in mass induced by `delta_mesh_coeff` are unlikely to exceed the typical 4% observational uncertainties. Similarly, radius uncertainties fluctuate at a level of approximately 0.02%, well below observational thresholds of 2% but not entirely negligible.

Fluctuations in $f_{\Delta\nu}$ induced by `delta_mesh_coeff`, however, are on the order of 0.02, which is comparable to those caused by other model physics (Pinsonneault et al. 2024). Hence, using the $\Delta\nu$ scaling relation with the model-based $f_{\Delta\nu}$ correction factors should be done carefully.

In the case of age, we find that resolution as a source of uncertainty is non-negligible, especially along the main sequence. A number of studies have examined the impact of modeling uncertainties—defined in various ways—on age determinations (e.g. Tayar et al. 2022; Joyce et al. 2023; Ying et al. 2023). The conclusion broadly shared by these investigations is that age error bars computed without modeling uncertainty considerations are heavily underestimated, and this study finds the same.

5.4. *Model Grid Emulators*

Several studies have aimed to emulate grids of stellar evolution calculations by approximating the relationships between stellar properties (e.g., mass, radius, age, oscillation frequencies) and model input parameters (e.g., initial mass, metallicity) using statistical models and machine learning techniques. These include methods such as normalizing flows (Hon et al. 2024), artificial neural networks (Mombarg et al. 2021; Scutt et al. 2023),

Gaussian Processes (Li et al. 2022a), and random forest (Bellinger et al. 2016). These approaches enable efficient interpolation across the complex and high-dimensional parameter space of model grids, producing smooth posteriors and significantly reducing computational costs (after the models are trained), enabling rapid parameter inference for large numbers of targets.

However, relatively few efforts have focused on achieving emulator precision significantly below observational uncertainties. One of the primary barriers to improving emulator precision is formally characterizing the numerical uncertainties inherent in the modeling process. This includes, but is not limited to, the effects of `delta_mesh_coeff` examined in this study.

6. BEST PRACTICES

We have shown that inadequate structural resolution can be highly problematic for asteroseismic analyses, parameter determinations, and evolutionary inferences based on p-modes. However, this source of uncertainty can be mitigated significantly (though not eliminated entirely) by adhering to a few key tenets of numerical modeling best practices:

1. Choose parameter settings thoughtfully.
2. Perform convergence tests.
3. Balance resolution against run time.

To the first of these points, the most obvious lesson from the present analysis is that the default structural resolution in `MESA`, `delta_mesh_coeff` = 1.0, is not adequate for many of the asteroseismic applications discussed in this paper. As a general rule, one should never assume that the default parameter values provided in tools like `MESA` and `GYRE` are optimized for science problems. More often, these settings are optimized to run models quickly for teaching or training purposes. As such, it is the user's responsibility to choose resolution values—and all other parameter settings—that are appropriate for their problem.

Per point two, convergence tests, or resolution studies, are a necessary part of modeling science. Results that are presented without demonstrating that the inferences and/or conclusions drawn from models are robust against resolution changes should not be trusted. Performing convergence tests also means making the results of those convergence tests available, whether via inclusion in an appendix or by publicly hosting the analysis code on a platform like GitHub.

Lastly, convergence does not have an absolute standard, but rather is defined relative to the precision needed for the result. In this sense, it is no better to set the structural resolution arbitrarily high than it is to inherit default settings blindly: things like structural and temporal resolution must always be balanced against run time (with higher-resolution models taking longer to run) and strain on numerical solvers, which often struggle more as resolution increases. A rule-of-thumb indicator that results are converged is if the answer does not change *within some reasonable tolerance* when the resolution is increased. The lowest resolution setting for which this is true is usually the optimal choice. Examples of "gold standard" convergence testing can be found in, e.g., Schootemeijer et al. (2019); Klencki et al. (2021) and Ziółkowska et al. (2024). Other studies that do not directly mention convergence testing but do use appropriate, non-default values of `delta_mesh_coeff` include Schmid & Aerts (2016); Buysschaert et al. (2018); Pedersen et al. (2018) and Johnston et al. (2024). This is by no means a comprehensive list.

Even when abiding by all best practices in numerical modeling, there will inevitably be some discrepancy, and therefore uncertainty, caused by resolution choices, just as there is uncertainty introduced by selecting a particular set of physical assumptions or a particular modeling tool. To account for correlated mode uncertainties in asteroseismic model fitting, we recommend constructing the χ^2 statistic using a covariance matrix, $\mathbf{C}$, as follows:

$$\chi^2 = (\nu_{\rm obs} - \nu_{\rm mod})^{\mathbf{T}} \mathbf{C}^{-1} (\nu_{\rm obs} - \nu_{\rm mod}), \qquad (15)$$

where $\nu_{\rm obs}$ and $\nu_{\rm mod}$ represent the observed and modeled frequencies, respectively.

In this formulation, the covariance matrix, $\mathbf{C}$, accounts for the fact that mode uncertainties are not independent. We propose that all elements of $\mathbf{C}$ be populated using $(\varepsilon_{\texttt{dmesh}})^2$. This ensures the inclusion of numerical uncertainties alongside observational noise in the fitting process. Incorporating a term like this may partially alleviate the need to manually down-weight seismic χ^2 constraints (e.g. Cunha et al. 2021) as a means of compensating for ultra-small observational uncertainties on individual p-mode measurements.

7. SUMMARY

In this study, we have quantified the impact of a factor-of-ten variation in the parameter `delta_mesh_coeff` on individual p-mode frequencies for solar-like, upper main-sequence, and Mira oscillators as well as a number of asteroseismic and fundamental stellar parameters derived from these modes. Using `MESA`'s default mesh size as the low-resolution reference point, we compared quantities determined at this resolution to those determined at a resolution 10x greater, introducing the quantities $\varepsilon_{\texttt{dmesh}}$ and $\zeta_{\texttt{dmesh}}$ as measures

of the discrepancy in frequency and period, respectively. These quantities serve as indicators of the uncertainty due to structural resolution. Our analysis required the development of a modified Equivalent Evolutionary Point (EEP) framework that can be readily adapted to study other forms of modeling uncertainty.

While solar-like oscillators typically had fractional uncertainties ($\varepsilon_{\texttt{dmesh}}/\nu_{\max}$) at or below 1% of the test frequency, fractional uncertainties in Miras ($\zeta_{\texttt{dmesh}}/P_{\text{test}}$) were as large as 20%. We found that structural resolution uncertainty was largest in models with higher masses, higher metallicities, and occupying later evolutionary stages. This is consistent with expectations given the more complicated interior physics of stars of these types.

We compared mesh resolution uncertainties to synthetic noise, σ_{obs}, computed for six TESS observing scenarios. In almost all cases uncertainty, $\varepsilon_{\texttt{dmesh}}$ ($\zeta_{\texttt{dmesh}}$) exceeded typical observational uncertainties, and often by many orders of magnitude. We computed the ratio of $\varepsilon_{\texttt{dmesh}}$ ($\zeta_{\texttt{dmesh}}$) to σ_{obs} for the worst-case observing scenario (T = 1 month, $\sigma_{\text{noise}} = 197$ ppm/hr) across all evolutionary tracks and found that the ratio was highest in roughly the same regions where absolute structural resolution uncertainty was largest.

When investigating the impact of resolution uncertainty on quantities influenced by or derived from p-modes, we found that the location and morphology of the RGB bump and red clump were impacted substantially. Of the global seismic parameters we studied, $\Delta\Pi_1$ was the most heavily affected.

When examining the influence of resolution uncertainty on fundamental stellar parameters, young main-sequence stars fared the worst: ages were impacted at the 10% level. Across models of nearly every evolutionary stage, $f_{\Delta\nu}$ fluctuated at the 2% level in response to changes in `delta_mesh_coeff`, which is at the same level as uncertainties induced by changing model physics.

Though we focus on p-mode asteroseismology in this analysis, our results clearly demonstrate the importance of incorporating resolution-based uncertainties into all asteroseismic applications. Currently, very few studies do. We strongly encourage a new standard in the field: when using models for asteroseismic analysis, take care to set `delta_mesh_coeff` (and related numerical parameters) appropriately, perform and publish convergence tests, and incorporate a mesh resolution term when quoting uncertainties.

Y. Li and M. Joyce contributed equally to this manuscript and may both refer to this as a first-author publication. The authors thank Jamie Tayar, Daniel Huber and László Molnár for fruitful discussions and valuable suggestions. Y. Li acknowledges support from Beatrice Watson Parrent Fellowship. M.J. gratefully acknowledges funding of MATISSE: *Measuring Ages Through Isochrones, Seismology, and Stellar Evolution*, project number 101038062, awarded through the European Commission's Widening Fellowship. This project has received funding from the European Union's Horizon 2020 research and innovation programme.

REFERENCES

Aerts C., 2021, Reviews of Modern Physics, 93, 015001
Aerts C., Christensen-Dalsgaard J., Kurtz D. W., 2010, Asteroseismology. Springer
Angelou G. C., D'Orazi V., Constantino T. N., Church R. P., Stancliffe R. J., Lattanzio J. C., 2015, MNRAS, 450, 2423
Auvergne M., et al., 2009, A&A, 506, 411
Bányai E., et al., 2013, MNRAS, 436, 1576
Bellinger E. P., Angelou G. C., Hekker S., Basu S., Ball W. H., Guggenberger E., 2016, ApJ, 830, 31
Borucki W. J., et al., 2010, Science, 327, 977
Broomhall A. M., et al., 2014, MNRAS, 440, 1828
Brown T. M., Gilliland R. L., Noyes R. W., Ramsey L. W., 1991, ApJ, 368, 599
Buysschaert B., Aerts C., Bowman D. M., Johnston C., Van Reeth T., Pedersen M. G., Mathis S., Neiner C., 2018, A&A, 616, A148
Campante T. L., et al., 2016, ApJ, 830, 138
Chaplin W. J., Miglio A., 2013, ARA&A, 51, 353
Chaplin W. J., et al., 2011, ApJ, 732, 54
Christensen-Dalsgaard J., 1984, in Mangeney A., Praderie F., eds, Space Research in Stellar Activity and Variability. p. 11
Christensen-Dalsgaard J., 2015, MNRAS, 453, 666
Christensen-Dalsgaard J., et al., 2020, A&A, 635, A165
Cinquegrana G. C., Joyce M., Karakas A. I., 2022, ApJ, 939, 50
Cinquegrana G. C., Joyce M., Karakas A. I., 2023, MNRAS, 525, 3216
Cunha M. S., et al., 2021, MNRAS, 508, 5864
Davies G. R., et al., 2015, MNRAS, 446, 2959
Dotter A., 2016, ApJS, 222, 8
Dréau G., Cunha M. S., Vrard M., Avelino P. P., 2020, MNRAS, 497, 1008

Dupret M. A., Grigahcène A., Garrido R., Gabriel M., Scuflaire R., 2005, A&A, 435, 927

Eddington A. S., 1926, The Internal Constitution of the Stars

Fraser A. E., Joyce M., Anders E. H., Tayar J., Cantiello M., 2022, ApJ, 941, 164

Gehan C., Mosser B., Michel E., Samadi R., Kallinger T., 2018, A&A, 616, A24

Gilliland R. L., et al., 2011, ApJS, 197, 6

Grevesse N., Sauval A. J., 1998, SSRv, 85, 161

Hacking P., et al., 1997, in Okuda H., Matsumoto T., Rollig T., eds, Astronomical Society of the Pacific Conference Series Vol. 124, Diffuse Infrared Radiation and the IRTS. p. 432

Hatt E. J., et al., 2024, MNRAS, 534, 1060

Henyey L., Vardya M. S., Bodenheimer P., 1965, ApJ, 142, 841

Hey D., Huber D., Ong J., Stello D., Foreman-Mackey D., 2024, arXiv e-prints, p. arXiv:2403.02489

Hon M., Li Y., Ong J., 2024, ApJ, 973, 154

Huber D., et al., 2011, ApJ, 743, 143

Huber D., et al., 2024, ApJ, 975, 19

Jermyn A. S., et al., 2023, ApJS, 265, 15

Johnston C., et al., 2024, ApJ, 964, 170

Joyce M., Chaboyer B., 2015, ApJ, 814, 142

Joyce M., Chaboyer B., 2018a, ApJ, 856, 10

Joyce M., Chaboyer B., 2018b, ApJ, 864, 99

Joyce M., Johnson C. I., Marchetti T., Rich R. M., Simion I., Bourke J., 2023, ApJ, 946, 28

Joyce M., Molnár L., Cinquegrana G., Karakas A., Tayar J., Tarczay-Nehéz D., 2024, ApJ, 971, 186

Karakas A. I., 2011, in Kerschbaum F., Lebzelter T., Wing R. F., eds, Astronomical Society of the Pacific Conference Series Vol. 445, Why Galaxies Care about AGB Stars II: Shining Examples and Common Inhabitants. p. 3

Khan S., Hall O. J., Miglio A., Davies G. R., Mosser B., Girardi L., Montalbán J., 2018, ApJ, 859, 156

Kiss L. L., Szabó G. M., Bedding T. R., 2006, MNRAS, 372, 1721

Kjeldsen H., Bedding T. R., 1995, A&A, 293, 87

Kjeldsen H., Bedding T. R., 2012, in Griffin E., Hanisch R., Seaman R., eds, IAU Symposium Vol. 285, New Horizons in Time Domain Astronomy. pp 17–22, doi:10.1017/S1743921312000142

Kjeldsen H., et al., 2005, ApJ, 635, 1281

Klencki J., Nelemans G., Istrate A. G., Chruslinska M., 2021, A&A, 645, A54

Kurtz D. W., 2022, ARA&A, 60, 31

Kuszlewicz J. S., Hon M., Huber D., 2023, ApJ, 954, 152

Li Y., Bedding T. R., Li T., Bi S., Stello D., Zhou Y., White T. R., 2020, MNRAS, 495, 2363

Li T., Davies G. R., Lyttle A. J., Ball W. H., Carboneau L. M., García R. A., 2022a, MNRAS, 511, 5597

Li T., Li Y., Bi S., Bedding T. R., Davies G., Du M., 2022b, ApJ, 927, 167

Li G., Deheuvels S., Ballot J., 2024a, A&A, 688, A184

Li Y., et al., 2024b, ApJ, 974, 77

Matthews J. M., et al., 2000, in Szabados L., Kurtz D., eds, Astronomical Society of the Pacific Conference Series Vol. 203, IAU Colloq. 176: The Impact of Large-Scale Surveys on Pulsating Star Research. pp 74–75

Merchan-Benitez P., Uttenthaler S., Jurado-Vargas M., 2023, A&A, 672, A165

Metcalfe T. S., et al., 2012, ApJL, 748, L10

Molnár L., Joyce M., Kiss L. L., 2019, ApJ, 879, 62

Mombarg J. S. G., Van Reeth T., Aerts C., 2021, A&A, 650, A58

Montalbán J., et al., 2021, Nature Astronomy, 5, 640

Murphy S. J., Joyce M., Bedding T. R., White T. R., Kama M., 2021, MNRAS, 502, 1633

Noll A., Basu S., Hekker S., 2024, A&A, 683, A189

Paxton B., Bildsten L., Dotter A., Herwig F., Lesaffre P., Timmes F., 2011, ApJS, 192, 3

Paxton B., et al., 2013, ApJS, 208, 4

Paxton B., et al., 2015, ApJS, 220, 15

Paxton B., et al., 2018, ApJS, 234, 34

Paxton B., et al., 2019, ApJS, 243, 10

Pedersen M. G., Aerts C., Pápics P. I., Rogers T. M., 2018, A&A, 614, A128

Pedersen M. G., et al., 2021, Nature Astronomy, 5, 715

Pinsonneault M. H., et al., 2024, arXiv e-prints, p. arXiv:2410.00102

Ricker G. R., et al., 2015, Journal of Astronomical Telescopes, Instruments, and Systems, 1, 014003

Roxburgh I. W., Vorontsov S. V., 2003, A&A, 411, 215

Schmid V. S., Aerts C., 2016, A&A, 592, A116

Schofield M., et al., 2019, ApJS, 241, 12

Schootemeijer A., Langer N., Grin N. J., Wang C., 2019, A&A, 625, A132

Scutt O. J., Murphy S. J., Nielsen M. B., Davies G. R., Bedding T. R., Lyttle A. J., 2023, MNRAS, 525, 5235

Sharma S., Stello D., Bland-Hawthorn J., Huber D., Bedding T. R., 2016, ApJ, 822, 15

Silva Aguirre V., et al., 2015, MNRAS, 452, 2127

Silva Aguirre V., et al., 2017, ApJ, 835, 173

Soszyński I., Wood P. R., Udalski A., 2013, ApJ, 779, 167

Tayar J., Joyce M., 2022, ApJL, 935, L30

Tayar J., Claytor Z. R., Huber D., van Saders J., 2022, ApJ, 927, 31

Tedersoo L., et al., 2021, Sci. Data, 8, 192
Townsend R. H. D., Teitler S. A., 2013, MNRAS, 435, 3406
Trabucchi M., Wood P. R., Montalbán J., Marigo P., Pastorelli G., Girardi L., 2017, ApJ, 847, 139
Trabucchi M., Mowlavi N., Lebzelter T., 2021, A&A, 656, A66
Verma K., Raodeo K., Basu S., Silva Aguirre V., Mazumdar A., Mosumgaard J. R., Lund M. N., Ranadive P., 2019, MNRAS, 483, 4678
Vrard M., Mosser B., Samadi R., 2016, A&A, 588, A87
White T. R., Bedding T. R., Stello D., Christensen-Dalsgaard J., Huber D., Kjeldsen H., 2011, ApJ, 743, 161
Xiong D. R., Deng L., Zhang C., Wang K., 2016, MNRAS, 457, 3163
Ying J. M., Chaboyer B., Boudreaux E. M., Slaughter C., Boylan-Kolchin M., Weisz D., 2023, AJ, 166, 18
Yu J., Bedding T. R., Stello D., Huber D., Compton D. L., Gizon L., Hekker S., 2020, MNRAS, 493, 1388
Zinn J. C., Pinsonneault M. H., Bildsten L., Stello D., 2023, MNRAS, 525, 5540
Ziółkowska O., Smolec R., Thoul A., Farrell E., Rathour R. S., Hocdé V., 2024, ApJS, 274, 30
de Meulenaer P., Carrier F., Miglio A., Bedding T. R., Campante T. L., Eggenberger P., Kjeldsen H., Montalbán J., 2010, A&A, 523, A54

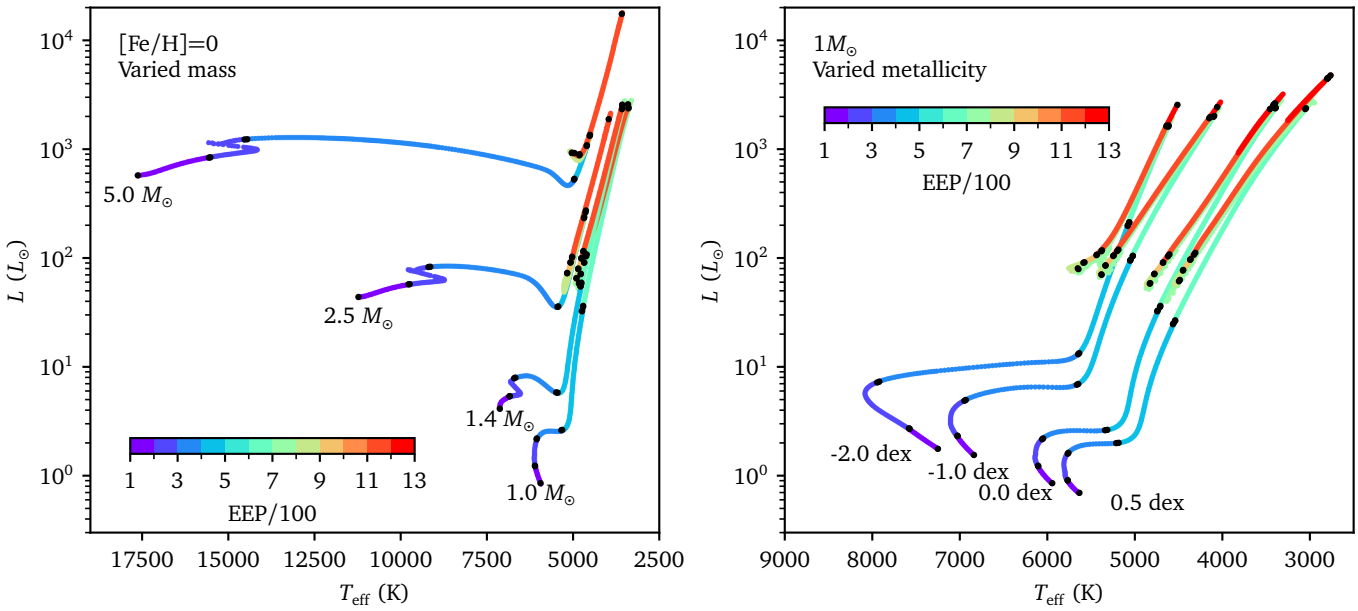

Figure 10. Evolutionary tracks used in this studied color-coded by the primary EEP values. The black dots show the critical points that separate primary EEPs.

APPENDIX

A. PRIMARY EEP

Figure 10 shows the stellar models on the H–R diagram, color-coded by their primary EEP.